

Fast and flexible long-range models for atomistic machine learning

Philip Loche,^{1,2} Kevin K. Huguenin-Dumittan,¹ Melika Honarmand,^{1,2} Qianjun Xu,¹ Egor Rumiantsev,^{1,2} Wei Bin How,^{1,2} Marcel F. Langer,¹ and Michele Ceriotti^{1,2}

¹Laboratory of Computational Science and Modeling, IMX, École Polytechnique Fédérale de Lausanne, 1015 Lausanne, Switzerland

²National Centre for Computational Design and Discovery of Novel Materials (MARVEL), École Polytechnique Fédérale de Lausanne, 1015 Lausanne, Switzerland^a

Most atomistic machine learning (ML) models rely on a locality ansatz, and decompose the energy into a sum of short-ranged, atom-centered contributions. This leads to clear limitations when trying to describe problems that are dominated by long-range physical effects – most notably electrostatics. Many approaches have been proposed to overcome these limitations, but efforts to make them efficient and widely available are hampered by the need to incorporate an ad hoc implementation of methods to treat long-range interactions. We develop a framework aiming to bring some of the established algorithms to evaluate non-bonded interactions – including Ewald summation, classical particle-mesh Ewald (PME), and particle-particle/particle-mesh (P3M) Ewald – into atomistic ML. We provide a reference implementation for *PyTorch* as well as an experimental one for *JAX*. Beyond Coulomb and more general long-range potentials, we introduce purified descriptors which disregard the immediate neighborhood of each atom, and are more suitable for general long-ranged ML applications. Our implementations are fast, feature-rich, and modular: They provide an accurate evaluation of physical long-range forces that can be used in the construction of (semi)empirical baseline potentials; they exploit the availability of automatic differentiation to seamlessly combine long-range models with conventional, local ML schemes; and they are sufficiently flexible to implement more complex architectures that use physical interactions as building blocks. We benchmark and demonstrate our *torch-pme* and *jax-pme* libraries to perform molecular dynamics simulations, to train ML potentials, and to evaluate long-range equivariant descriptors of atomic structures.

I. INTRODUCTION

Machine learning (ML) has become essential in atomistic simulations, especially as a surrogate for quantum mechanical methods like density functional theory (DFT). Early works by Behler and Parrinello¹ and Bartók et al.² demonstrated that ML models are able to predict the energy and forces of an atomic structure at close to DFT accuracy with significantly reduced computational cost. Since then, the field has rapidly expanded in many directions: On one hand, various architectures including kernel-based approaches^{2–4} and message-passing neural networks have emerged to further improve accuracy and efficiency^{5–9}. Furthermore, beyond just the energy or other rotationally invariant target properties, the field has seen the rise of equivariant model architectures that can also handle tensorial target properties such as dipoles and polarizabilities^{10–12}, the electron density^{13–15}, the Hamiltonian operator^{16,17} and many-particle wavefunctions^{18–20}. Thanks to the mathematical field of representation theory, there is now a systematic understanding about how to incorporate any type of behavior under rotations in ML models^{21–23}.

Despite these advancements, a persistent limitation in many of the ML models is the use of finite cutoff radii, which had been justified in terms of the “nearsightedness of electronic matter”^{24,25}. While this allows for efficient methods with computational costs that scale lin-

early with the number of atoms, the trade-off is the introduction of systematic errors in scenarios where long-range interactions play a crucial role. For instance, electrostatic interactions from the direct Coulomb potential to induced multipolar interactions are critical in ionic and polar materials, affecting dielectric constants, phonon spectra, and structural stability^{26–28}. Dispersion (van der Waals) forces are equally vital in layered materials, molecular crystals and interfaces, as they contribute to cohesion and adhesion energies^{29–31}. Ignoring these interactions in ML models restricts their applicability.

This work presents libraries for the *PyTorch* and *JAX* frameworks that implement efficient methods for computing a family of long-range features as well as classical long-range energy corrections in an automatically differentiable manner. Due to the use of popular and flexible ML libraries, the features can easily be integrated into any pre-existing ML framework for invariant and equivariant target properties, with or without gradients.

In section II, we begin by providing an overview of the scientific background concerning algorithms for long-range electrostatics developed by the molecular dynamics (MD) community, as well as long-ranged ML methods. In section III, we discuss some of the specific technical choices and the core features of our implementation. In section IV, we demonstrate and benchmark our reference *torch-pme* implementation in several different use cases, providing also some comparisons with its more experimental *jax-pme* companion.

^a)These two authors contributed equally.

II. BACKGROUND

Long-range interactions are not new to ML, and have in fact already been studied extensively since the outset of traditional atomistic simulations. Here we briefly summarize the key ideas.

A. Notation and Conventions

In this subsection, we focus on the Coulomb potential, and define the bare potential function

$$v(r) = \frac{1}{r} \quad (1)$$

for $r \in (0, \infty)$, even though the general setting of the problem applies to any pair potential, and we will discuss a few concrete cases of other $1/r^p$ -type interactions for more general exponents $p > 0$. In a system of N atoms with positions $\mathbf{r}_i \in \mathbb{R}^3$ and weights (charges) q_i for $i = 1, \dots, N$, the Coulomb potential V_i at the location of an atom i and the total energy E of the system can be defined as

$$V_i = \frac{1}{2} \sum_{j \neq i} q_j v(r_{ij}) \quad (2)$$

$$E = \sum_{i=1}^N q_i V_i, \quad (3)$$

where $r_{ij} = \|\mathbf{r}_i - \mathbf{r}_j\|$ is the distance between atoms i and j , and we also include the factor of 1/2 to account for double-counting directly in the definition of V_i .

We can extend the atomic potentials to periodic systems by also including all interactions with periodic images of the atoms. Thus,

$$V_i = \frac{1}{2} \sum_{j=1}^N \sum_{\mathbf{l}}' q_j v(\|\mathbf{r}_i - \mathbf{r}_j - \mathbf{l}\|), \quad (4)$$

where \mathbf{l} runs over the lattice vectors of the periodic cell. The sum over j also includes $i = j$ in the periodic case to take into account the interactions between atom i and its own periodic images. For this special case of $i = j$, the prime symbol in the second summation sign indicates that the term with $\mathbf{l} = 0$ must be omitted to avoid the singularity in v as $r \rightarrow 0$.

While conceptually straight-forward, this definition of the potential in periodic space is problematic for the Coulomb potential since its slow decay makes the sum over \mathbf{l} conditionally convergent. A naive implementation (such as spherical summation) does not even converge³².

B. Ewald Summation

Ewald summation, published in 1921, remains a foundational method that effectively defines how to extend

this computation to periodic systems³³. The proposed solution is to perform a range separation of the Coulomb potential: We write

$$v(r) = v_{\text{SR}}(r) + v_{\text{LR}}(r) \quad (5)$$

$$v_{\text{SR}}(r) = \frac{\text{erfc}\left(\frac{r}{\sqrt{2}\sigma}\right)}{r} \quad (6)$$

$$v_{\text{LR}}(r) = \frac{\text{erf}\left(\frac{r}{\sqrt{2}\sigma}\right)}{r}, \quad (7)$$

where σ is a ‘‘smearing’’ parameter that defines the range separation and erf (erfc) is the (complementary) error function $\text{erf}(x) = 2/\sqrt{\pi} \int_0^x \exp(-t^2) dt$ (and $\text{erfc}[x] = 1 - \text{erf}[x]$). The first term v_{SR} contains the singularity of the Coulomb potential as $r \rightarrow 0$ and decays quickly as $r \rightarrow \infty$. Thus, we call this the short-range part of the Coulomb potential. v_{LR} on the other hand decays as $1/r$ as $r \rightarrow \infty$ just like the Coulomb potential, but remains smooth and finite for $r \rightarrow 0$. We call it the long-range part of the Coulomb potential. The transition between the two happens roughly at $r \approx \sigma$. We will shortly discuss how to choose σ in practice.

Using this range separation, the potential of atom i can be written as

$$V_i = \frac{1}{2} \sum_{j=1}^N \sum_{\mathbf{l}}' q_j v_{\text{SR}}(\|\mathbf{r}_i - \mathbf{r}_j - \mathbf{l}\|) \quad (8)$$

$$+ \frac{1}{2} \sum_{j=1}^N \sum_{\mathbf{l}}' q_j v_{\text{LR}}(\|\mathbf{r}_i - \mathbf{r}_j - \mathbf{l}\|). \quad (9)$$

Due to the fast decay of v_{SR} , the sum over j and \mathbf{l} in the first term converges quickly. We can thus efficiently implement it by introducing a cutoff radius r_{cut} , and only summing up the contributions up to this distance.

The second sum is still conditionally convergent, since v_{LR} contains the slowly decaying behavior of the Coulomb potential. However, since the singularity as $r \rightarrow 0$ has been removed, v_{LR} is now a smooth function and hence has a quickly decaying Fourier transform given by

$$\hat{v}_{\text{LR}}(k) = \frac{4\pi}{k^2} e^{-\frac{1}{2}\sigma^2 k^2}; \quad (10)$$

$k = \|\mathbf{k}\|$ is the norm of the reciprocal space vector \mathbf{k} .

We can now use the Poisson summation formula, which allows us to convert a sum over a periodic lattice into a dual sum in reciprocal space. The details on the used conventions for Fourier transforms and a proof of the Poisson summation formula for the convenience of readers can be found in section S1 of the supporting information. The

final result for the potential of atom i is

$$V_i = V_{i,\text{SR}} + V_{i,\text{LR}} + V_{i,\text{self}} + V_{i,\text{charge}} \quad (11)$$

$$V_{i,\text{SR}} = \frac{1}{2} \sum_{j=1}^N \sum_{\mathbf{l}}' q_j v_{\text{SR}}(\|\mathbf{r}_i - \mathbf{r}_j - \mathbf{l}\|) \quad (12)$$

$$V_{i,\text{LR}} = \frac{1}{2\Omega} \sum_{j=1}^N \sum_{\mathbf{k} \neq 0} q_j \hat{v}_{\text{LR}}(k) e^{i\mathbf{k}(\mathbf{r}_i - \mathbf{r}_j)} \quad (13)$$

$$V_{i,\text{self}} = -\frac{1}{2} q_i \sqrt{\frac{2}{\pi}} \frac{1}{\sigma} \quad (14)$$

$$V_{i,\text{charge}} = -\frac{\pi \sigma^2 Q}{\Omega}, \quad (15)$$

where Ω is the volume of the unit cell, the sum over \mathbf{k} is a sum over all nonzero reciprocal space lattice vectors and $Q = \sum_i q_i$ is the total charge of all atoms in the unit cell. We have kept the overall factor of 1/2 that arises from double counting at the front for better comparison with results from some authors which handle this factor differently. The extra term $V_{i,\text{charge}}$ is required to enforce charge neutrality, a requirement of the method. If the provided charges q_i do not lead to a charge-neutral cell, a homogeneous background charge is added to the system to ensure overall neutrality in the unit cell. The term is then the interaction between an atom and this background charge. $V_{i,\text{self}} = q_i v_{\text{LR}}(0)/2$ is the self-term which compensates the interaction of an atom with itself via v_{LR} , which is an artifact of the reciprocal space sum.

Due to the fast decay of $\hat{v}_{\text{LR}}(k)$ as $k \rightarrow \infty$, the long-range sum can now also be computed efficiently by choosing a cutoff k_{cut} and truncating the sum by only including terms for which $k \leq k_{\text{cut}}$. The naive Ewald algorithm has a computational cost scaling quadratically with the number of atoms, $\mathcal{O}(N^2)$, while optimizations – letting r_{cut} scale with the size of the unit cell – can bring the exponent in the scaling down to $\mathcal{O}(N^{3/2})$ ³⁴.

C. Generalization to Arbitrary Exponents

This work has been extended a few decades later to other interactions beyond the Coulomb potential, including more general power-law potentials $v(r) = 1/r^p$ with an interaction exponent $p > 0$ ^{35–38}. The Coulomb interaction corresponds to $p = 1$, while dispersion corresponds to $p = 6$. Summarizing their results using our conventions and notations, the range separation $v = v_{\text{SR}} + v_{\text{LR}}$ is performed using

$$v_{\text{SR}}(r) = \frac{1}{\Gamma(\frac{p}{2})} \frac{\Gamma(\frac{p}{2}, \frac{r^2}{2\sigma^2})}{r^p} \quad (16)$$

$$v_{\text{LR}}(r) = \frac{1}{\Gamma(\frac{p}{2})} \frac{\gamma(\frac{p}{2}, \frac{r^2}{2\sigma^2})}{r^p} \quad (17)$$

$$\hat{v}_{\text{LR}}(k) = \frac{\pi^{3/2} 2^{3-p} \Gamma(\frac{3-p}{2}, \frac{1}{2}\sigma^2 k^2)}{\Gamma(\frac{p}{2}) k^{3-p}}, \quad (18)$$

where $\Gamma(a) = \int_0^\infty t^{a-1} e^{-t} dt$ is the (complete) Gamma function, $\Gamma(a, x) = \int_x^\infty t^{a-1} e^{-t} dt$ is the upper incomplete Gamma function and $\gamma(a, x) = \Gamma(a) - \Gamma(a, x) = \int_0^x t^{a-1} e^{-t} dt$ the lower incomplete Gamma function. Up to a prefactor, we see that the functional form of \hat{v}_{LR} is identical to v_{SR} , the difference being that r/σ gets replaced by σk and p by $3-p$. This high degree of symmetry is one reason that makes this particular choice of v_{SR} efficient. Note that we use a custom implementation of the incomplete Gamma functions that, contrary to the one present in *PyTorch*, supports integer exponents up to $p = 6$.

To get the atomic potentials, the decomposition

$$V_i = V_{i,\text{SR}} + V_{i,\text{LR}} + V_{i,\text{self}} + V_{i,\text{charge}} \quad (19)$$

is still valid, where the first two terms are computed using the identical method but using the generalized expressions for v_{SR} and \hat{v}_{LR} , while

$$V_{i,\text{self}} = -\frac{q_i}{2} \frac{1}{(2\sigma^2)^{\frac{p}{2}} \Gamma(\frac{p}{2} + 1)} \quad (20)$$

$$V_{i,\text{charge}} = -\frac{\pi^{\frac{3}{2}} (2\sigma^2)^{\frac{3-p}{2}} Q}{(3-p) \Gamma(p/2) \Omega}. \quad (21)$$

We remark that the self-term is always necessary for any exponent $p \in (0, \infty)$. The charge correction term, on the other hand, should only be used for $p < 3$. This is because, only for these slowly decaying potentials, the energy diverges if the cell is not “charge-neutral”, thus requiring the addition of a homogeneous background, while for $p > 3$ this is not the case. The critical case $p = 3$ is more subtle, but we treat it just like $p > 3$, i.e. by setting $V_{i,\text{charge}} = 0$. A derivation of these two correction terms with a more detailed discussion of their subtleties can be found in the supporting information section S2. Note that neither of the terms depends on the particle positions, and hence do not affect gradients or forces.

D. Mesh-Based Approaches

The Ewald sum provided the first absolutely convergent formulation for the potential in a periodic system, and remains important to this day. It suffers, however, from a relatively inefficient computational scaling with the number of atoms. Thus, many algorithms have been developed to significantly reduce the computational cost of the Ewald sum, enabling the use of long-range methods for the simulation of large-scale systems. The most important family for this work consists of the particle-mesh methods, such as particle-particle particle-mesh (P3M) which was published first^{39,40}, the original particle mesh Ewald (PME)⁴¹ and its extension called smooth PME (SPME)⁴². These methods use the fast Fourier transform (FFT)⁴³ to perform the reciprocal space part of the Ewald sum, and bring the asymptotic scaling of the computational cost down to $\mathcal{O}(N \log N)$. They assume peri-

odicity in the system, but can also be used for aperiodic systems with some care and modifications⁴⁴.

The key idea is that the two sums appearing in Equation 13 can “almost” be interpreted as discrete Fourier transforms: We can in fact break down the computation of $V_{i,\text{LR}}$ into the two sums

$$\hat{q}(\mathbf{k}) = \sum_{j=1}^N q_j e^{-i\mathbf{k}\mathbf{r}_j} \quad (22)$$

$$V_{i,\text{LR}} = \sum_{\mathbf{k} \neq 0} \hat{q}(\mathbf{k}) \hat{v}_{\text{LR}}(k) e^{i\mathbf{k}\mathbf{r}_i}. \quad (23)$$

Both Equation 22 and Equation 23 look quite similar to Fourier transforms, but with one key difference: The positions \mathbf{r}_i and \mathbf{r}_j are in general not equally spaced. Thus, despite the apparent similarity, these cannot directly be computed using algorithms for the discrete Fourier transform.

The similarity however motivates the following trick: In order to use the efficient FFT algorithm, we can interpolate the weights q_i onto an equally-spaced mesh. This generates an effective (charge) density ρ that is only defined on the mesh. While this changes the position of the particles, and hence introduces discretization errors, the regular nature of the particle positions now allows us to compute the appropriately modified versions of both Equation 22 and Equation 23 efficiently using three-dimensional FFT. The computational cost typically scales as $\mathcal{O}(N \log N)$, assuming a fixed mesh spacing and that the system volume is proportional to the number of atoms. This general description and scaling is common to all mesh-based methods.

The PME, P3M and SPME methods simply differ in (1) the choice of interpolation scheme between the particle positions and the mesh, (2) the choice of \hat{v}_{LR} that is used in Equation 23, and (3) the method to perform the differentiation to compute the electric field or forces. We briefly summarize the first two key distinguishing points for PME and P3M, as these are particularly relevant for this work. Deserno and Holm⁴⁰ provide a more detailed discussion.

The original version of PME⁴¹ is the simplest for both (1) and (2). The interpolation is performed using (piecewise) Lagrange interpolation, a well-known technique in numerical analysis⁴⁵. Furthermore, \hat{v}_{LR} remains the same as for the Ewald summation, Equation 10 for Coulomb and Equation 18 for the general case. It can in fact be shown that for this choice of \hat{v}_{LR} , the Lagrange interpolation scheme is optimal regarding the discretization errors arising due to the mesh⁴⁰.

This is the simplest of the three variants to implement, and therefore serves as a convenient testing ground for new implementations. One key downside, however, is that the interpolation scheme leads to non-smooth behavior or even discontinuities even for arbitrarily high interpolation orders⁴⁰, making the method less suitable for our approach that fully exploits the automatic differentiation capabilities of *PyTorch* and *JAX*. The authors

of PME have in fact addressed this issue by presenting the SPME algorithm just two years after the original version⁴².

The P3M algorithm, despite being more complex than the original PME, was historically presented first. It is widely used due to its superior accuracy⁴⁰. The key idea is that in a periodic system, the effective Coulomb potential or Green’s function is different than in vacuum due to the periodic neighbors. This is what suggests a modification of \hat{v}_{LR} by taking into account the periodic cell. Since the crystal lattice breaks rotation symmetry, $\hat{v}_{\text{LR}}(\mathbf{k})$ no longer is spherically symmetric and now depends on the three-dimensional vector \mathbf{k} rather than just its norm k . In practice, \hat{v}_{LR} is obtained by minimizing an estimated force error due to discretization. P3M further uses a custom interpolation scheme that is obtained from requiring a smooth interpolation. The combination of the interpolation scheme and optimized \hat{v}_{LR} makes P3M more accurate, and hence a popular choice despite its higher complexity compared to naive PME.

Beyond the mesh-based ones, many other algorithms have been developed to efficiently compute electrostatic interactions, including the fast multipole method that was the first linear-scaling, $\mathcal{O}(N)$ method for electrostatics^{46,47}. Despite the better asymptotic scaling and hence faster speed as $N \rightarrow \infty$, the larger prefactor typically makes the particle-mesh methods more suitable for the large system sizes of $N = 10^3 \sim 10^5$, which is why, in this work, we focus on particle-mesh methods rather than fast multipole methods.

E. Long-Range ML Models

Inspired by these developments for long-range interactions in the last century, it has become increasingly popular for ML models in atomistic modeling to incorporate long-range corrections as well. In fact, one of the founding works by Bartók et al.² already included an explicit dispersion term in the prediction of the energy for GaAs structures. A similar strategy has been used by many subsequent works^{48–52}, in which the energy and optionally the forces of a structure are predicted as the sum of a more sophisticated ML part and an explicit long-range term of the form $1/r^p$. Typically, each chemical species is assigned a fixed weight (or charge in the case of Coulomb interactions) in these interactions. This makes it simple to train the models, and has the advantage that it can be combined with essentially any model architecture.

In the last five years, the field has also seen the rise of more sophisticated approaches going beyond simple point charge models to handle more complex datasets. One extension is to make the particle weights or charges themselves dependent on the atomic environments^{53,54}, and to learn this relationship directly from the data. Alternatively, it has been proposed to learn the positions of the Wannier centers^{55–57}. This allows the center of the electron charge to be different from the positively

charged ion, naturally capturing dipolar effects. Alternatively, it is possible to learn electronegativities rather than the charges, and to compute the charges from a subsequent charge equilibration scheme^{58–61}. This approach has the advantage that the final charges can depend on atoms beyond a local cutoff, and hence can capture non-local charge transfer. A general property of these methods is that they are most naturally designed to have the energy (and forces) as the target property. This specialization makes the methods very powerful for this task, but less suitable to other target properties. In addition, the original implementation lacked efficiency and scalability, but this was recently resolved by also using a mesh paradigm⁶¹ improving the scaling significantly.

While these approaches work well to incorporate electrostatic energy corrections, there are two common deficits. First, being explicitly designed to reproduce physical interactions, they are not necessarily well-suited for the data-driven modeling of long-range effects with a different origin, or affecting a property other than the energy. Second, even though they are designed to incorporate long-range interactions, the numerical value of the quantities they compute is dominated by short-range contributions. This happens because even though the Coulomb potential (or more general power-laws) at the position of an atom depend on atoms that are far away, they are still primarily determined by neighbor atoms that are close by. This contamination by short-range terms can be compensated by the presence of a conventional short-range ML model, but goes against the notion of treating the two parts separately.

An alternative approach, developed by some of the authors in this work, emphasizes constructing general equivariant features that encode long-range information, rather than focusing directly on the energy as a target property^{62–64}. These long-distance equivariant (LODE) features can be applied in various ML models to predict a range of target properties, from scalar invariants to higher-order equivariants. While prior studies have primarily explored the method’s capabilities, the implementation used an Ewald-like summation approach⁶⁴, leading to an $\mathcal{O}(N^2)$ scaling. This quadratic scaling limits the method’s applicability to larger systems.

As is the case for the usual Coulomb potential, LODE in its original formulation is not a range separated descriptor, but contains all short-range (i.e., within cutoff) and long-range contributions of a system. To address this issue, we will introduce the exterior potential features (EPFs) in the next section, which is a modification of the original formulation that only includes the contributions from exterior atoms^{64,65}. A similar idea has already been applied to LODE features in previous work⁶⁴. In addition, recently there is strong evidence^{61,66,67} that using a full spherical expansion of the potential is not necessary to describe long-range effects in machine learning models, but so far there is no rigorous investigation of these observations. A mathematical motivation thereof is provided in section S3 of the supporting information,

which also connects the approaches in this work with our previous work.

III. METHOD

Our primary goal is to design a library to compute long-range interactions that can be easily integrated with existing short-range architectures, essentially providing an easy-to-use framework to build range separated models for atomistic machine learning. To this end, our reference *torch-pme* library provides

1. A modular implementation of range separated potentials working for arbitrary unit cells including triclinic ones.
2. Full integration with *PyTorch*, featuring differentiable and learnable parameters,
3. Efficient particle-mesh-based computation with automatic hyperparameter tuning,
4. Pure long-range descriptors, free of short-range contributions,
5. Support for arbitrary invariant and equivariant features and ML architectures.

We discuss these features in general terms, without focusing too much on the specific Application Programming Interface (API), because similar ideas can be readily implemented with other ML frameworks, as we are currently doing with an experimental *jax-pme* library.

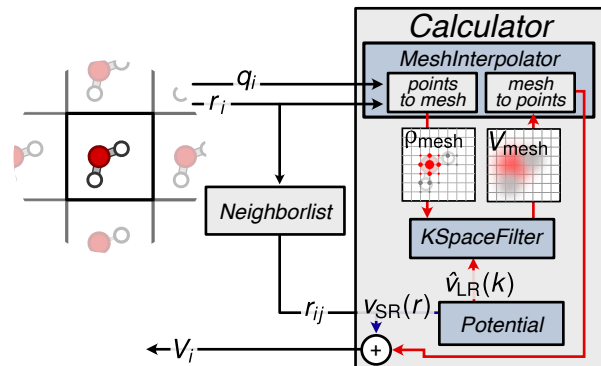


Figure 1. A schematic representation of the main building blocks inside a *Calculator* of a range separated architecture, that combines an evaluation of the short-range part of the potential $v_{\text{SR}}(r)$ based on local interatomic distance information with the evaluation of the long-range part $v_{\text{LR}}(k)$ using grids via a *MeshInterpolator* and a *KSpaceFilter*.

A. A modular implementation of range separated models

As discussed in section II, the key concept underlying all efficient methods to model long-range interactions

is to split the calculation of the pair interactions between two particles into a short and long-range part, i.e., $v(r) = v_{\text{SR}}(r) + v_{\text{LR}}(r)$. The short-range part, which decays to (effectively) zero beyond a set cutoff distance r_{cut} , is computed by summing over the neighbors of each particle. The neighbor-list required for the pair distances r_{ij} in the short-range part have to be calculated with an external library. These pairs are also needed for any short-range component of a ML model, and can be easily precomputed during training. The long-range part is computed in k -space, based on its Fourier transform $\hat{v}_{\text{LR}}(k)$ and requires the absolute position vectors \mathbf{r}_i as well as the particle weights q_i (that correspond to charges for an electrostatic potential). Furthermore, the methods with an efficient scaling in the asymptotic limit, such as PME or P3M, convert the particle-based description into a smooth particle density, discretizing it on a real-space mesh, and using FFT to perform a Fourier convolution.

These ingredients can be used for more general tasks than computing explicitly physical interatomic potentials. To make this possible, our implementation follows a modular design, in which a *Potential* class exposes methods to compute $v(r)$, $v_{\text{SR}}(r)$, $v_{\text{LR}}(r)$, $\hat{v}_{\text{LR}}(k)$; a *Mesh-Interpolator* converts particle positions \mathbf{r}_i and pseudo-charges q_i into a density mesh, and vice-versa interpolates a scalar field defined on the mesh at arbitrary positions; a *KSpaceFilter* performs the Fourier-domain convolution.

These elements can be combined in a *Calculator* object that applies one of the classical algorithms to compute long-range interactions, evaluating the potential at the atomic positions, $V_i = V(\mathbf{r}_i)$ (see Figure 1). However, the same modular components can also be used in more complex ways. For example, users can compute descriptors based on the local potential in a neighborhood around each atom, such as LODE^{62,64} features (section IV E).

As long as all components are implemented within an auto-differentiable framework, both the base calculators and any custom architecture allows to easily evaluate derivatives of the predictions with respect to particle coordinates, cell matrix, and model parameters.

B. Fully Differentiable and Learnable Framework

In practice, the integration of long-range calculators with ML libraries built around automatic evaluation of gradients makes it easy to combine long-range terms with any *PyTorch*- and *JAX*-based ML model. This includes optimizing parameters such as the particle weights q_i and even the type of interaction itself by e.g. parametrizing the interaction as $v(r) = w_1/r + w_2/r^2 + w_3/r^3$, where w_1 , w_2 , and w_3 are learnable. This flexibility is illustrated for both simple toy systems (section IV C) and complex model architectures (section IV D). Automatic differentiation also makes the implementation of models that learn both the energies and forces effortless.

C. Hyperparameter Tuning

Range-separated calculations like Ewald summation and its mesh-based variants require careful distribution of the computational load between the real-space and the Fourier-space contributions. This is relevant both for computational performance and correctness; poor choices of parameters can lead to severe errors of the potential and the forces, while over-emphasizing correctness can result in prolonged computational time. Parameters to be optimized include the mesh spacing and the real-space interaction cutoff. Our package comes with a parameter tuning functionality that simplifies the process for non-experts for the Coulomb potential based on known estimates for the force error \mathcal{E}_F ^{68–70}. To this end, the relevant parameters, which we call θ , are optimized to fulfill the target accuracy requirement, i.e. $\mathcal{E}_F(\theta) < \epsilon_{\text{target}}$, while taking the shortest computational time.

The accuracy can be set by the user, with some default suggestions. The cutoff r_{cut} is set to a fixed value by the user. In principle, the cutoff can also be optimized but its value is usually fixed by a short range machine learning model. The smearing σ is optimized to achieve a real space error equal to $\epsilon_{\text{target}}/2$ using a closed-form estimate of the error. For the remaining parameters related to the k -space evaluation, a grid search is performed using a set of heuristically determined parameters. The force error estimate \mathcal{E} also depends on the algorithm used, as its k -space part is different for Ewald summation, PME, and P3M. A mock computational speed test is performed for each set of parameters fulfilling the accuracy requirement. Further details and the concrete mathematical expressions can be found in section S4 of the supporting information. Benchmark results in section IV A demonstrate and compare the obtained accuracy with the desired value ϵ_{target} , as well as the resulting speed.

D. Exterior potential features

When computing physical interactions, the potential generated on a central atom i by a set of N atoms with weights q_j at distances r_{ij} can be expressed as

$$V_i^{\text{full}} = \frac{1}{2} \sum_{j \neq i} q_j v(r_{ij}), \quad (24)$$

where $p > 0$ is the exponent associated with the interaction, e.g., $p = 1$ for Coulomb and $p = 6$ for dispersion forces. The sum can be performed explicitly for a finite system, while a more general definition is necessary in the periodic case, as discussed in section II. This atom-centered potential contains information on the position of atoms in the far-field. It is however not an ideal descriptor of long-range interactions: Despite being physically motivated, it also contains short-range effects from particles in the vicinity of the atom of interest.

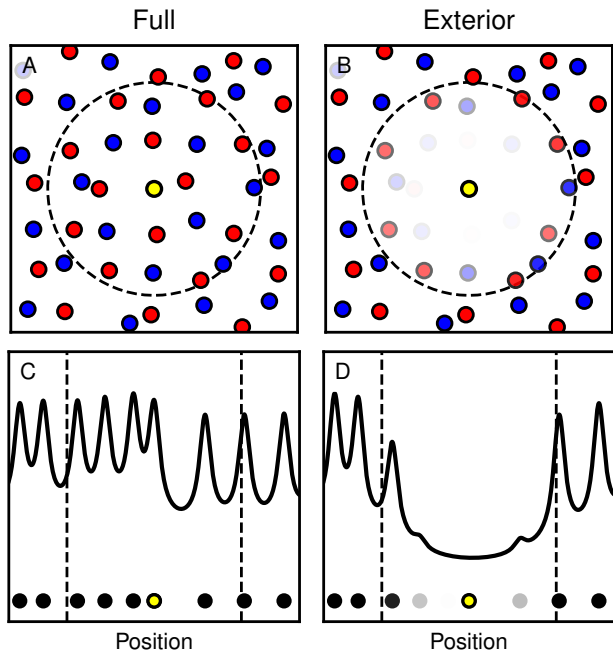


Figure 2. Schematic representation of the atoms contributing to the full potential (A) and exterior potential features (B). Each circle represents an atom that contributes to the potential of the center atom shown in yellow, with the cutoff circle shown as a dotted line. In the latter case, the contribution of interior atoms is gradually turned on as their distance approaches the cutoff. Panels (C) and (D) show a one-dimensional example, where the vertical axis now shows the Coulomb potential (smeared out to remove the singularity) generated by the atoms. The large difference in the potential curve with and without the interior contributions shows how the electrostatic potential around an atom is mostly dominated by its immediate neighbors, despite the long-range nature of the Coulomb potential.

In practice, short-ranged ML models are already excellent at extracting short-ranged information from neighbor atoms up to a cutoff radius $r_{\text{cut}} > 0$. To realize “range separated”, multi-scale models, it is therefore preferable to obtain purely long-ranged features. We introduce “exterior potential features” (EPFs)

$$V_i^{\text{ext}} = \frac{1}{2} \sum_{r_{ij}} q_j f_{\text{trans}}(r_{ij}) v(r_{ij}) \quad (25)$$

$$\approx \frac{1}{2} \sum_{r_{ij} > r_{\text{cut}}} q_j v(r_{ij}) \quad (26)$$

that eliminate the contributions from atoms within the cutoff, which are already well-modeled by the short-range part of the model (see Figure 2A and B). The transition function f_{trans} essentially eliminates the contribution from interior atoms, but does so in a smooth way to ensure the differentiability of the features as atoms leave or enter the interior region. In the current implementation,

it is explicitly given by

$$f_{\text{trans}}(r) = \begin{cases} \left[1 - \cos\left(\frac{r^n}{r_{\text{cut}}^n}\right)\right] / 2 & r < r_{\text{cut}} \\ 0 & r \geq r_{\text{cut}}, \end{cases} \quad (27)$$

with some exponent n that controls how quickly the contributions of the interior atoms vanishes as they approach the cutoff.

To illustrate the benefit of the exterior variant, consider the electrostatic (Coulomb) potential generated by a one-dimensional chain of Gaussian charge distributions. Figure 2C shows the construction leading to the full features, while Figure 2D corresponds to the exterior variant. The stark difference in the two curves around the location of the center atom i shows that even for the very slowly decaying Coulomb potential, the potential around an atom is most strongly influenced by the immediate neighbors. If the goal is to obtain long-ranged features to combine them with a short-ranged model, we can see that the exterior variant offers a clean signal, while the full potential features are contaminated by the redundant short-range contributions. *torch-pme* provides an implementation of this idea, similar to a construction that has already been used in our previous work⁶⁴. This is a key difference with approaches that are based on the explicit modeling of physical interactions. In the following paragraphs, all examples use standard full potentials unless stated otherwise. Additionally, every time EPFs are mentioned, they are always used in the form that incorporates the smooth f_{trans} function.

E. Implementing range separated ML architectures

There are two main approaches one can take to incorporate long-range terms in an ML architecture. One involves re-purposing traditional range separated calculators to evaluate potential-like values at the atomic positions, and combine them with short-range model architectures to compute short-range interactions, atomic pseudo-charges, or arbitrary non-linear combinations of local descriptors and atom-centered potentials. Given that the atom-centered potential values are (in the limit of a converged mesh) translationally and rotationally invariant, this approach can be easily applied to make invariant or equivariant predictions. In addition, a full separation of a short and long-range model allows using multiple time stepping schemes to further reduce the overhead stemming from the long-range evaluation^{71,72}.

The second approach exploits the fact that mesh-based range separated calculators return the potential values on a grid that covers the entire system. This makes it possible to evaluate equivariant atom-centered features (along the lines of the LODE framework^{62,64}) and combine them with equivariant local descriptors within an equivariant architecture.

Even though the latter approach is more general (and can be used, for instance, to describe many-body non-

covalent interactions⁶⁴) analytical considerations indicate that the most important information on long-range pair interactions is contained in the invariant part of the descriptors (see also the SI for a more thorough discussion). For this reason, the core components of the library we developed focus on the evaluation of invariant features, which facilitate constructing fast, flexible and streamlined range separated models. Nevertheless, the *torch-pme* API does allow to evaluate fully equivariant LOD features quite easily, as we show in section IV E.

IV. BENCHMARKS AND MODEL ARCHITECTURES

Having discussed some of the general principles, and the overall structure of our implementation, we now move on to discuss some practical examples and benchmarks. If not stated otherwise, all presented results are obtained using the *torch-pme* implementation with single precision (32 bit) floating point arithmetics. In section IV A we begin by presenting benchmarks on the speed and accuracy of the implementation. To further validate the correct behavior of the “full potential” for more complex systems, section IV B presents MD trajectories in which our algorithms have been used to compute the electrostatic forces via a LAMMPS interface, and compare the results against LAMMPS’s own P3M implementation. In order to showcase the flexibility of *torch-pme*, section IV C illustrates how our implementations easily allows learning different interaction types and charges. Beyond these toy systems, section IV D provides an example of a more involved model architecture, and compares the results to previous work. Finally, section IV E discusses how to use the building blocks of *torch-pme* to evaluate more complicated equivariant features.

A. Benchmark: Speed and Accuracy

We begin by discussing the results on the automatic hyperparameter tuning, as this also determines the parameters used for the remaining tests on speed and accuracy. For many simple crystal structures, lattice energies assuming purely electrostatic interactions and ideal formal charges (commonly referred to as Madelung constants) are known and tabulated with great accuracy. We define the actual (relative) accuracy as

$$\epsilon_{\text{true}} = \frac{|E_{\text{actual}} - E_{\text{reference}}|}{E_{\text{reference}}}, \quad (28)$$

where E_{actual} is the obtained energy and $E_{\text{reference}}$ are the tabulated reference energies. Figure 3 show the relative accuracy of the predicted energies after tuning the parameters for the Ewald summation and the mesh calculators in single precision (32-bit) floating point arithmetics for a given desired accuracy $\epsilon_{\text{desired}} = \Delta F/F_{qq}$, where F_{qq} is the constant force created by two elementary charges

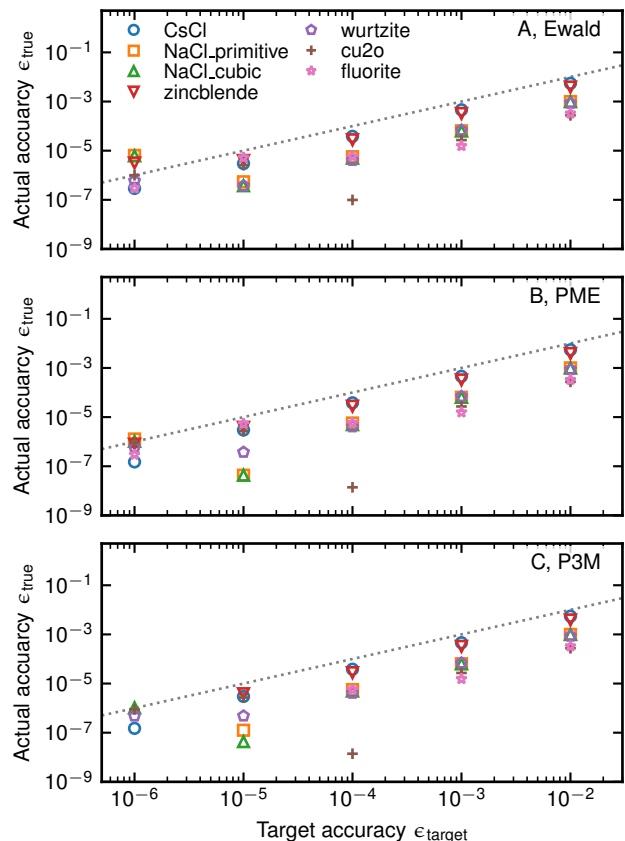


Figure 3. Empirical versus target accuracy after tuning calculator parameters for different replicated crystal structures and long-range methods using single precision floating point numbers. Panels show results for Ewald (A), PME (B) and P3M (C). Each crystal was replicated 32 times in each direction from its initial unit cell structure until. Different colored symbols represent different crystals. The true target accuracies are obtained from reference Madelung constants^{73,74}.

separated by 1Å to convert absolute errors into an estimated relative error as is also done in LAMMPS. We compute and show results for a few high-symmetry crystal structures with tabulated Madelung constants^{73,74}. The unit cell was replicated 32 times in each direction, so that each structure contains at least 10,000 atoms. For each structure, the actual accuracy ϵ_{true} is plotted against the desired accuracy ϵ_{target} , meaning that ideally, all points should lie below the black dotted line defined by $\epsilon_{\text{true}} = \epsilon_{\text{desired}}$. Computation were performed on a single AMD EPYC 9334 CPU and one NVIDIA H100 SXM5 GPU showing. In Fig. S6 in the supplementary material we show that a very similar behavior is observed for double-precision arithmetics.

For a diverse dataset containing structures with different numbers of atoms, we recommend tuning the parameters on the system with the largest cell and largest number of particles. A more detailed discussion of these considerations, as well as more detailed plots on the auto-

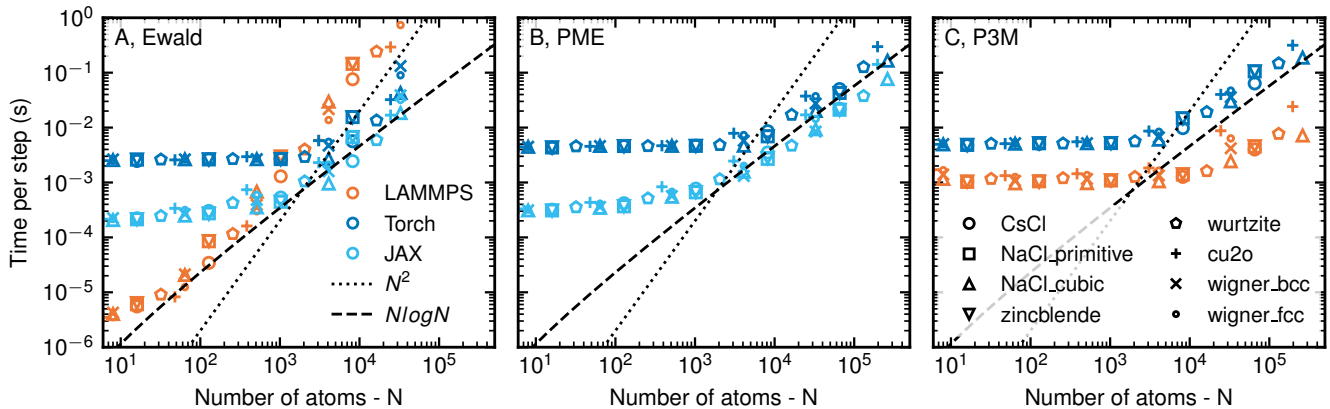


Figure 4. Benchmark for computational cost of long-range calculators to run a single point evaluation of the energy, force and stress for different replicated crystal structures. Panels show results for Ewald (A) PME (B) and P3M (C). Different crystals are shown as different symbols. Each point is an average of 50 single point calculations of the same positions with a tuning accuracy of $1 \cdot 10^{-4}$. Calculations for *torch-pme* and *jax-pme* were performed with single precision (32-bit).

tuning of the parameters and the convergence can be found in the supporting information.

Accuracy is only one aspect of a successful implementation. In Figure 4, we demonstrate that *torch-pme* and *jax-pme* are also competitive in terms of computational cost by comparing them against LAMMPS’s Ewald and P3M implementations using the same replicated crystal structures shown in Figure 3. The LAMMPS benchmarks were performed using the version from August 2, 2023 (Update 3), in combination with the Kokkos 4.3.1 package. For our Ewald and P3M benchmarks, we used the same parameters optimized by LAMMPS, to ensure a fair comparison of the implementation. For a relative force accuracy of 10^{-4} the LAMMPS parameters differ by less than 10% when comparing to parameters obtained by our own tuning code. For PME we tune a separate set of parameters, aiming for an absolute force accuracy of 10^{-4} . In all cases, we employed a fixed cutoff of 4.4 \AA , which provided the best performance for our largest structure, containing approximately 263’000 atoms in a cubic cell with a side length of 65 \AA (see section S5 for a visualization of the grid search used to determine this cutoff value). All reported timings include only the evaluation of the short- and long-range components of the Coulomb potential, as well as its derivatives. Notably, they do not account for the computation of the neighbor list. This exclusion is justified because, in typical machine learning applications, the long-range part of the architecture is often combined with a short-range one, whose neighbor list can usually be reused. Additionally, in MD applications, the neighbor list can be reused for multiple timesteps.

Figure 4 shows that for small system sizes up to about $N = 1000$ atoms, LAMMPS Ewald (Figure 4A) is the fastest implementation, followed first by the Ewald method in *jax-pme* and then the PME method in *jax-pme*, and finally *torch-pme*. We can see that the cost for our implementation is more or less constant across this

range, meaning that this is not due to an inefficiency in the actual algorithm, but rather a general overhead required during the initialization. Even though these overheads are hard to quantify, they are probably related to better CUDA kernel initialization and dispatch to the GPU by *JAX*. After a transition region between $N = 10^3$ and $N = 10^4$, we observe that our Ewald implementations outperform the LAMMPS one, while all codes show the expected scaling of $\mathcal{O}(N^2)^{34}$. In principle, one can tune the Ewald method to $\mathcal{O}(N^{3/2})$ scaling by setting $\sigma \propto N^{1/6}$ and deducing the real and Fourier space cutoffs accordingly. We show this scaling in the supplementary material in Fig. S7. However, this scaling cannot be achieved in a usual machine learning workflow where the cutoff is fixed by the short-range model. The mesh-based algorithms are competitive with the LAMMPS P3M implementation, while also showing the correct scaling of $\mathcal{O}(N \log N)^{34}$. For a system size of $N = 10^4$, the mesh-based algorithms are already faster than the Ewald ones by a factor of about five, with the gap widening quickly due to the $\mathcal{O}(N^2)$ asymptotic scaling of the latter. From these observations, we conclude that the implementations are fast enough for most practical applications. We further recommend using the Ewald method during training, which usually involves small structures, where Ewald is faster than PME. After training, and when running production simulations, one should switch to the PME or P3M calculators to achieve the best performance for larger systems. Note that switching between the Ewald and mesh-based (PME and P3M) calculators is unproblematic as both can be tuned to achieve high, and consistent, accuracy as demonstrated in Figure 3, and share fully compatible APIs. As discussed further in the supplementary material, section S6, none of the benchmarked implementations are able to fully utilize available hardware on a modern GPU. We therefore expect further performance optimization to yield significant im-

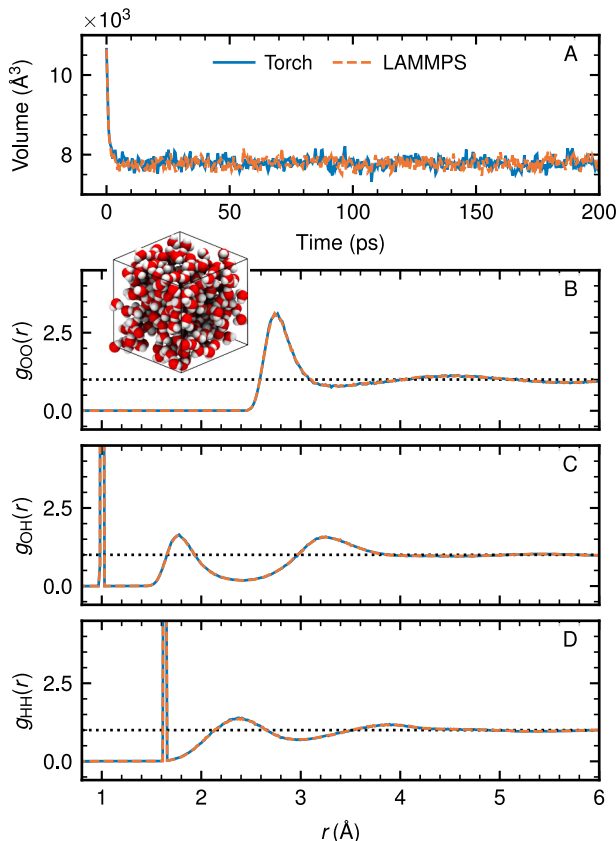


Figure 5. A: Time series of the first 200 ps showing the fluctuating volume of an NpT simulation of rigid SPC/E water. The Coulombic part of the interactions are either handled by *torch-pme*'s implementation of PME (blue) or LAMMPS's P3M implementation (red). B – D: Oxygen-oxygen $g_{OO}(r)$, oxygen-hydrogen $g_{OH}(r)$ and hydrogen-hydrogen $g_{HH}(r)$ radial distribution functions. The inset in B shows a snapshot of the initial configuration

provements.

B. Molecular Dynamics

Even though *torch-pme* is designed with ML applications in mind, it is a good sanity check to verify it can be used as an empirical force-field engine. To this end, we construct a model that evaluates the electrostatic contributions for a rigid SPC/E water model⁷⁵, while the Lennard-Jones contributions are handled by the simulation engine. For such a model, no training is performed since the charges for the SPC/E model are fixed ($-0.8476 e$ for oxygen and $0.4238 e$ for hydrogen). We use the Metatensor framework⁷⁶ to export a *Torchscript* model that can be loaded and executed within the LAMMPS simulation engine⁷⁷. We then perform a 2 ns NpT simulation of $N = 256$ rigid water molecules. The time step of the simulation is set to 2 fs and the posi-

tions are recorded every 200 steps (0.2 ps). Temperature is controlled using the CSV thermostat⁷⁸ and the pressure using a Nosé-Hoover barostat. During the simulation the Coulomb interaction between the particles was either handled by LAMMPS or the *torch-pme* implementation, both using hyperparameters whose (absolute) accuracy have been converged to $\epsilon = 2 \cdot 10^{-5} \text{ kcal/mol/\AA}$. Note that any of the grid-based implementations could also be used, but our benchmarks show that, since the number of atoms is still small ($N < 1000$), the Ewald implementation is faster. In Figure 5 (a) we show the time evolution of the system volume, in which the cell equilibrates from the initial configuration (a cubic cell with a side of 22 Å), reaching the same equilibrium volume. From the volume fluctuations we can compute the isothermal compressibility

$$\kappa_T = -\frac{1}{V} \left. \frac{\partial V}{\partial p} \right|_T. \quad (29)$$

The literature value for SPC/E water is $\kappa_{T,\text{ref}} = (4.6 \pm 0.2) \cdot 10^{-10} \text{ m}^2 \text{ N}^{-179}$ which agrees well with our result of $\kappa_T = (4.8 \pm 0.3) \cdot 10^{-10} \text{ m}^2 \text{ N}^{-1}$ for *torch-pme*, and $\kappa_{T,\text{LAMMPS}} = (4.7 \pm 0.1) \cdot 10^{-10} \text{ m}^2 \text{ N}^{-1}$ for pure LAMMPS. We obtain our values by leaving out the first 10 ps of the simulation for equilibration and calculate the error by a block average over 10 blocks. In Figure 5B to D, we show the radial distribution function between the two methods, which are essentially identical.

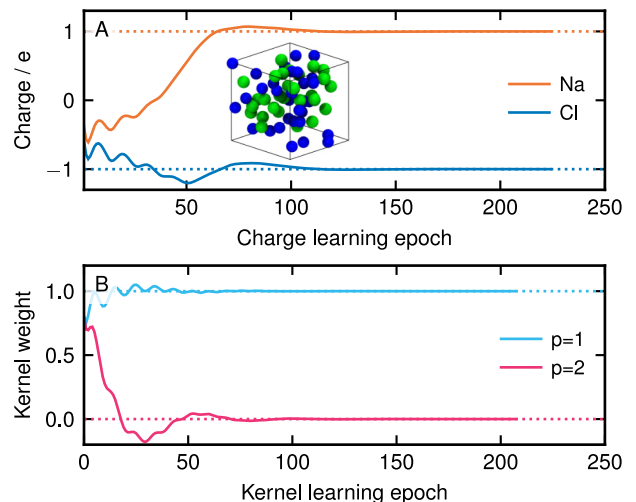


Figure 6. Training curves for the charge of the sodium and chloride atoms optimized on the energy of 10 random structures (A) and for optimizing the prefactor of two Fourier space kernels with different exponents p (B). The inset in A shows one snapshot of the structures in the training set.

C. Learning charges and potentials

To illustrate how to use *torch-pme* as a flexible module for machine learning tasks, we design two toy examples that demonstrate the possibility of optimizing atomic pseudo-charges, and the functional form of the pair interactions. For both, we use a dataset of 1000 NaCl structures each consisting of $N = 64$ randomly placed atoms in cubic boxes of various side lengths that was already used in previous work^{62,64}. Half of the atoms are Na atoms and assigned a fixed charged of $q_{\text{Na}} = +1$, while the other half are Cl atoms with a charge of $q_{\text{Cl}} = -1$. The total energy and forces of the systems are then computed assuming a pure Coulomb interaction between the atoms with an external reference calculator.

In both of the models that we discuss, the optimization was performed using the Adam optimizer with a maximum learning rate of $2 \cdot 10^{-1}$ as implemented in *PyTorch*. In the first model, we make the atomic charges q_{Na} and q_{Cl} learnable parameters, and initialize them to a small but non-zero value. Note that we do not explicitly enforce charge neutrality, even though it could help for more complex systems. The two charges are then optimized by fitting on the energy of the structures. Figure 6 (a) shows the charges as a function of the number of epochs in the training procedure. We can see that even though the convergence is not monotonic, the charges reach the correct values after in fewer than 100 epochs.

In the second model, we fix $q_{\text{Na}} = +1$ and $q_{\text{Cl}} = -1$ but this time modify the interaction potential to be of the form

$$v(r|w_1, w_2) = \frac{w_1}{r} + \frac{w_2}{r^2}, \quad (30)$$

with learnable weights w_1 and w_2 . Figure 6 (b) shows the evolution of these weights, again as a function of the number of epochs. We can see that after about 1000 epochs, both weights converge to the expected, reference values of $w_1 = 1$ and $w_2 = 0$. Example files that were used to run these calculations are provided as examples in the package repositories and documentation.

D. A model with learnable local charges

To demonstrate a more realistic application, we developed a complete end-to-end machine learning model (Figure 7A) and evaluated its performance on the organic molecules dataset used in our previous work⁶⁴ containing 2291 molecular pairs of 22 relaxed organic molecules in vacuum separated by various distances up to 15 Å in a periodic cell of 30 Å. This represents just one example among the many possible model architectures that can be constructed using *torch-pme*. This particular model has the overall structure of a ‘‘third-generation’’ neural network potential⁸⁰. It predicts the potential energy of a system, which we decompose into atom-wise energy contributions: $E_{\text{system}} = \sum_{i=1}^N E_i$, where E_{system}

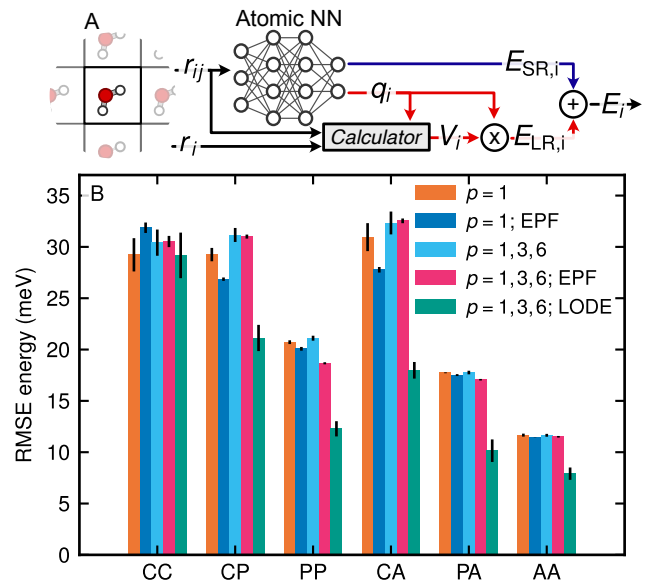


Figure 7. Schematic representation of an architecture that combines an atomic NN with a range separated calculator (A) and bar plots showing the comparison of RMSE on energies for different test subsets with error bars indicating the uncertainty estimated from 5 training runs

(B): charge-charge (CC), charge-polar (CP), polar-polar (PP), charge-apolar (CA), polar-apolar (PA), apolar-apolar (AA). Orange bars represent results from the architectures taken from Ref. 64 while all other bars represent results from the architecture described in panel (A).

is the total potential energy of the system, N is the number of atoms, and E_i represents the energy contribution from a single atom. We further decompose the atom-wise energy into short-range (SR) and long-range (LR) components: $E_i = E_{\text{SR},i} + E_{\text{LR},i}$. The SR part is computed using an atomic Neural Network (NN) which takes as input an invariant descriptor representing the local atomic environment within a predefined cutoff radius r_{cut} : $E_{\text{SR},i} = f_{\theta^{\text{SR}}}^{\text{SR}}(\xi_i)$ where ξ_i is a vector describing the environment of atom i and θ represents the learnable parameters of the function f_{θ}^{SR} . For our implementation, we used the Smooth Overlap of Atomic Positions (SOAP)² parameterization with the same parameters as in Ref 64. The NN consists of three layers, each with 256 neurons. Training was conducted for 200 epochs using the Adam optimizer with the OneCycleLR policy⁸¹ and a maximum learning rate of $5 \cdot 10^{-4}$. Besides predicting the $E_{\text{SR},i}$ the same model predicts also the atomic charges $q_i = f_{\theta^{\text{charge}}}^{\text{charge}}(\xi_i)$, which serve as inputs to a *torch-pme* Calculator to compute the long-range potential V_i and energy $E_{\text{LR},i} = q_i \cdot V_i$. In Figure 7B, we show a comparison of the results obtained using our pipeline. Specifically, we consider four cases for V_i : (1) using the full Coulomb potential ($p = 1$), (2) using the Coulomb EPFs ($p = 1$; EPF), (3) using a linear combination of the Coulomb potential with a $1/r^3$ and $1/r^6$ term with

learnable weights ($p = 1, 3, 6$), and (4) using the same linear combination as in (3) but with EPFs instead of the full potential features. We compare our results to those from Ref. 64, where LODE descriptors were employed which includes on the order of 10^3 features per atom, whereas our current pipeline generates only a single descriptor. We find that we achieve similar accuracy for the subset containing interactions between charged fragments, which is the dominating contribution in the dataset. However, we tend to perform slightly worse on other subsets, as these are no longer dominated by simple Coulomb-like interactions. This discrepancy is unsurprising because the LODE descriptors use more features to effectively capture other long-range interactions beside the Coulombic ones. Similar to what was observed in Ref. 64, the inclusion of additional exponents (e.g., $p = 3$ and 6 in our case) does not yield better results. Combined with learnable charges, a single descriptor restricted to long-range information is sufficient to capture the most prominent energy contributions, and that there isn't sufficient data to learn the weaker interactions with high accuracy. Note that the errors are largest for the CC pairs, since the Coulomb interaction is largest in absolute terms, consistently with our previous findings⁶⁴. Further improvements would likely require more sophisticated architectures, which we are planning to explore in future work. Finally, we observe that using EPFs provides only a marginal improvement in most cases (except for the charge-charge pair, where a decrease in accuracy is expected due to the EPFs breaking strict physical description). For this simple model and small dataset, whether or not E_{LR} contains short-range contributions is not as relevant as these can be compensated by the flexibility of E_{SR} . A clear-cut range separation is still very useful – e.g. to accelerate the evaluation of the model with multiple time stepping^{71,72} – and it may prove beneficial in more complex models, or when used for long-range effects that are not dominated by electrostatics.

E. Long distance equivariant features

As an example of how modular design and automatic differentiation help adapt classical algorithms for long-range interactions to modern machine learning tasks, we discuss how to evaluate long-distance equivariant (LODE) features. A concise summary of the basic idea behind LODE⁶², and its generalization to $1/r^p$ potentials⁶⁴, is provided in Fig. 1 of Ref. 64. In essence, it consists of first computing the potential $V(\mathbf{r}) = \sum_i q_i v(|\mathbf{r} - \mathbf{r}_i|)$ generated by the atoms with weights q_i , and then to expand it in an atom-centered basis

$$V_{in} = \int V(\mathbf{r}) B_n(\mathbf{r} - \mathbf{r}_i) d\mathbf{r}, \quad (31)$$

where B_n are a set of basis functions. Usually, the basis functions are factorized in radial functions and spherical

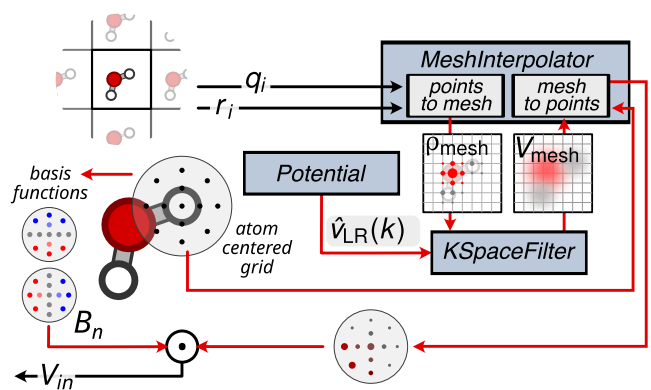


Figure 8. A schematic representation of the architecture of a model that computes LODE features, by evaluating the long-range part of the potential on a real-space grid, interpolating it on atom-centered grids, and combining it with a set of basis functions to evaluate atom-centered descriptors V_{in} , that are rotationally equivariant as long as the chosen basis functions are.

harmonics, but this is inconsequential from the point of view of the implementation (see Fig. 8).

The first step involves computing $V(\mathbf{r})$ on a real-space grid. This can be achieved with a Fourier convolution, exactly as in a grid-based long-range calculator. A subtlety is that it is less convenient to include a short-range correction, because one would have to evaluate it at all grid points, and not only at atomic positions, requiring one to build an additional neighbor list and to compute a much larger number of real-space pair interactions. Alternatively, and given that the objective is to build long-range *descriptors* rather than to compute a precise physical interaction, one can exclusively use v_{LR} and compute only the reciprocal space component. If one wants to do this while also subtracting the interior contribution, the cutoff function has to be included in the computation of \hat{v}_{LR} . Given that this cannot be done analytically for a general, smooth cutoff function, we implement a potential based on real-space cubic splines, which is numerically processed to generate the Fourier kernel.

After having obtained $V(\mathbf{r})$ on a regular mesh, we have to evaluate the integral (31). To do so, one can define an atom-centered mesh within a sphere with the desired radius, and interpolate the potential at the grid points. Then, the integral can be performed as a dot product with the basis function, pre-computed on the same grid, and appropriate quadrature weights. Given that the *MeshInterpolator* class allows interpolating on arbitrary points, this architecture can be realized very easily, and the resulting method is quite fast given that the basis functions are pre-computed at initialization, competitive with the existing implementations of LODE⁸² also for systems of moderate size.

V. CONCLUSIONS

We have presented a highly flexible framework to perform long-range ML efficiently, and provide two reference implementations in *PyTorch* and *JAX*. Our method allows us to compute not only electrostatic and more general inverse power-law potentials of the form $1/r^p$, but also to produce purified descriptors that exclusively contain information about atoms outside of the cutoff radius. This is useful when combining these features with short-range ML models, and can be used to predict any invariant or equivariant target property. The features can be computed using a variety of methods: Ewald summation is well-suited for small to moderate system sizes with hundreds of atoms, while the particle-mesh algorithms such as PME and P3M scale almost linearly with system size, $\mathcal{O}(N \log N)$, and are hence well-suited for larger structures. All calculators fully support arbitrary unit cells, from cubic to triclinic ones. We provide a real space direct calculator for free boundary conditions systems and also plan extending our libraries using algorithms for 1D and 2D periodic systems^{83–86}.

Our reference implementation fully exploit the flexibility and automatic differentiation capabilities of the *PyTorch* and *JAX* libraries, allowing for smooth integration into any pre-existing ML architecture. We also provide functions to automatically tune the numerical parameters of the methods, further streamlining ease of use, with benchmarks confirming the competitive speed and accuracy of the implementations. Besides the direct application to improve existing short-range models, our implementations also allow an easier inclusion of applied external potentials or fields into machine learning models^{11,87}. The modular structure also allows for various modifications for power-users who wish to fully exploit the flexibility of the implementations. We hope that the availability of these libraries will encourage the development of more standardized, efficient and scalable long-range ML models, and that their modular design will allow to develop more flexible, general models than the simple point-charge examples we discuss here.

VI. SUPPLEMENTARY MATERIAL

The electronic supporting material for this publication include further details on the implementation, different models and datasets, and additional results on benchmarks. The source code *torch-pme* and *jax-pme* packages are publicly available at <https://github.com/lab-cosmo/torch-pme> and <https://github.com/lab-cosmo/jax-pme>. Some results are compared with the generalized LODE descriptors introduced in previous work by the authors, which have been computed using the *featomic* (formerly *rascaline*) package⁸², available at <https://github.com/metatensor/featomic>.

ACKNOWLEDGMENTS

MC, KKHD, MFL, PL and WBH acknowledge funding from the European Research Council (ERC) under the research and innovation programme (Grant Agreement No. 101001890-FIAMMA). MC, PL, ER and MH acknowledge funding from the NCCR MARVEL, funded by the Swiss National Science Foundation (SNSF, grant number 182892), which also supported a research internship for MH through an Inspire Potentials Fellowship. MFL acknowledges funding from the German Research Foundation (DFG) under project number 544947822. We would like to thank the members of the Laboratory of Computational Science and Modeling, and especially Guillaume Fraux, Filippo Bigi and Arslan Mazitov, for their contributions to the software infrastructure that enabled this study. We further thank Philipp Stärk for useful discussions.

DATA AVAILABILITY STATEMENT

The source code to our *PyTorch* and *JAX* libraries are available on Github at <https://github.com/lab-cosmo/torch-pme> and <https://github.com/lab-cosmo/jax-pme>. All presented results have been computed using version 0.2 of *torch-pme* and commit db1e662b of *jax-pme*. Code to reproduce Figure 6 as well as how to construct LODE densities are available as tutorials in the *torch-pme* documentation. The datasets used in this work are taken from our previous work⁶⁴ and can either be found in its supporting information, or more directly at the *materialscloud* database entry <https://archive.materialscloud.org/record/2023.151>. All other codes and input files for computing the accuracies, running benchmarks, MD simulations, and the model with learnable local charges are as well available on Zenodo at <https://zenodo.org/records/14792591>.

REFERENCES

- ¹J. Behler and M. Parrinello, “Generalized neural-network representation of high-dimensional potential-energy surfaces,” *Physical Review Letters* **98**, 146401 (2007).
- ²A. P. Bartók, M. C. Payne, R. Kondor, and G. Csányi, “Gaussian approximation potentials: The accuracy of quantum mechanics, without the electrons,” *Physical Review Letters* **104**, 136403 (2010).
- ³M. Rupp, A. Tkatchenko, K.-R. Müller, and O. A. von Lilienfeld, “Fast and accurate modeling of molecular atomization energies with machine learning,” *Physical Review Letters* **108**, 058301 (2012).
- ⁴K. T. Schütt, H. E. Sauceda, P.-J. Kindermans, A. Tkatchenko, and K.-R. Müller, “SchNet – a deep learning architecture for molecules and materials,” *The Journal of Chemical Physics* **148**, 241722 (2018).
- ⁵K. T. Schütt, P.-J. Kindermans, H. E. Sauceda, S. Chmiela, A. Tkatchenko, and K.-R. Müller, “SchNet: A continuous-filter convolutional neural network for modeling quantum interac-

- tions,” *Advances in Neural Information Processing Systems* **30** (2017).
- ⁶J. Klicpera, S. Giri, J. T. Margraf, and S. Günnemann, “Directional message passing for molecular graphs,” *International Conference on Learning Representations* (2020).
 - ⁷L. Zhang, J. Han, H. Wang, R. Car, and W. E, “Deep potential molecular dynamics: A scalable model with the accuracy of quantum mechanics at the cost of classical molecular dynamics,” *Physical Review Letters* **120**, 143001 (2018).
 - ⁸N. Thomas, T. E. Smidt, S. Kearnes, L. Yang, L. Li, K. Kohlhoff, and P. Riley, “Tensor field networks: Rotation- and translation-equivariant neural networks for 3d point clouds,” arXiv preprint arXiv:1802.08219 (2018).
 - ⁹A. Musaelian, S. Batzner, A. Johansson, L. Sun, C. J. Owen, M. Kornbluth, and B. Kozinsky, “Learning local equivariant representations for large-scale atomistic dynamics,” *Nat Commun* **14**, 579 (2023).
 - ¹⁰A. Glielmo, P. Sollich, and A. De Vita, “Accurate interatomic force fields via machine learning with covariant kernels,” *Physical Review B* **95**, 214302 (2017).
 - ¹¹A. Grisafi, D. M. Wilkins, G. Csányi, and M. Ceriotti, “Symmetry-adapted machine learning for tensorial properties of atomistic systems,” *Physical Review Letters* **120**, 036002 (2018).
 - ¹²D. M. Wilkins, A. Grisafi, Y. Yang, K. U. Lao, R. A. DiStasio Jr., and M. Ceriotti, “Accurate molecular polarizabilities with coupled cluster theory and machine learning,” *Proceedings of the National Academy of Sciences* **116**, 3401–3406 (2019).
 - ¹³F. Brockherde, L. Vogt, L. Li, M. E. Tuckerman, K. Burke, and K.-R. Müller, “Bypassing the kohn-sham equations with machine learning,” *Nature Communications* **8**, 872 (2017).
 - ¹⁴A. Fabrizio, A. Grisafi, B. Meyer, and C. Corminboeuf, “Electron density learning of non-covalent systems,” *Chemical Science* **10**, 9424–9432 (2019).
 - ¹⁵A. J. Lewis, A. Grisafi, M. Ceriotti, and M. Rossi, “Learning electron density in the condensed phase,” *Journal of Chemical Theory and Computation* **17**, 6725–6737 (2021).
 - ¹⁶K. T. Schütt, M. Gastegger, A. Tkatchenko, K.-R. Müller, and R. J. Maurer, “Unifying machine learning and quantum chemistry with a deep neural network for molecular wavefunctions,” *Nature Communications* **10**, 5024 (2019).
 - ¹⁷E. Cignoni, D. Suman, J. Nigam, L. Cupellini, B. Mennucci, and M. Ceriotti, “Electronic excited states from physically constrained machine learning,” *ACS Central Science* **10**, 637–648 (2024), <https://doi.org/10.1021/acscentsci.3c01480>.
 - ¹⁸G. Carleo and M. Troyer, “Solving the quantum many-body problem with artificial neural networks,” *Science* **355**, 602–606 (2017).
 - ¹⁹J. Hermann, Z. Schätzle, and F. Noé, “Deep-neural-network solution of the electronic schrödinger equation,” *Nature Chemistry* **12**, 891–897 (2020).
 - ²⁰O. T. Unke, M. Bogojeski, M. Gastegger, M. Geiger, T. Smidt, and K.-R. Müller, “SE(3)-equivariant prediction of molecular wavefunctions and electronic densities,” (2021), arXiv:2106.02347.
 - ²¹W. Fulton and J. Harris, *Representation Theory: A First Course*, Graduate Texts in Mathematics, Vol. 129 (Springer-Verlag, New York, 1991).
 - ²²J.-P. Serre, *Linear Representations of Finite Groups*, Graduate Texts in Mathematics, Vol. 42 (Springer-Verlag, New York, 1977).
 - ²³M. Tinkham, *Group Theory and Quantum Mechanics* (Dover Publications, Mineola, NY, 2003) originally published in 1964 by McGraw-Hill.
 - ²⁴W. Kohn, “Density functional and density matrix method scaling linearly with the number of atoms,” *Phys. Rev. Lett.* **76**, 3168–3171 (1996).
 - ²⁵E. Prodan and W. Kohn, “Nearsightedness of electronic matter,” *Proceedings of the National Academy of Sciences* **102**, 11635–11638 (2005), <https://www.pnas.org/content/102/33/11635.full.pdf>.
 - ²⁶C. J. Fennell and J. D. Gezelter, “Is the ewald summation still necessary? pairwise alternatives to the accepted standard for long-range electrostatics,” *Journal of Chemical Physics* **124**, 234104 (2006).
 - ²⁷M. Born and K. Huang, “Dynamical theory of crystal lattices,” Oxford University Press (1954).
 - ²⁸J. D. Jackson, *Classical Electrodynamics Third Edition*, 3rd ed. (Wiley, New York, 1998).
 - ²⁹S. Grimme, “Semiempirical gga-type density functional constructed with a long-range dispersion correction,” *Journal of Computational Chemistry* **27**, 1787–1799 (2006).
 - ³⁰A. Tkatchenko and M. Scheffler, “Accurate molecular van der waals interactions from ground-state electron density and free-atom reference data,” *Physical Review Letters* **102**, 073005 (2009).
 - ³¹R. A. DiStasio, V. V. Gobre, and A. Tkatchenko, “Many-body van der waals interactions in molecules and condensed matter,” *Journal of Physics: Condensed Matter* **26**, 213202 (2014).
 - ³²J. M. Borwein, M. L. Glasser, R. C. McPhedran, J. G. Wan, and I. J. Zucker, *Lattice Sums Then and Now*, Encyclopedia of Mathematics and its Applications (Cambridge University Press, 2013).
 - ³³P. P. Ewald, “Die Berechnung optischer und elektrostatischer Gitterpotentiale,” *Annalen der Physik* **369**, 253–287 (1921).
 - ³⁴M. P. Allen and D. J. Tildesley, *Computer Simulation of Liquids* (Oxford University Press, 2017).
 - ³⁵B. R. A. Nijboer and F. W. De Wette, “On the calculation of lattice sums,” *Physica* **23**, 309–321 (1957).
 - ³⁶D. E. Williams, “Accelerated convergence of crystal-lattice potential sums,” *Acta Crystallographica Section A* **27**, 452–455 (1971).
 - ³⁷D. E. Williams, “Accelerated Convergence Treatment of R-n Lattice Sums,” *Crystallography Reviews* **2**, 3–23 (1989), publisher: Taylor & Francis eprint: <https://doi.org/10.1080/08893118908032944>.
 - ³⁸N. Karasawa and W. A. Goddard III, “Acceleration of convergence for lattice sums,” *The Journal of Physical Chemistry* **93**, 7320–7327 (1989).
 - ³⁹R. W. Hockney and J. W. Eastwood, “Computer simulation using particles,” CRC Press (1981).
 - ⁴⁰M. Deserno and C. Holm, “How to mesh up Ewald sums. I. A theoretical and numerical comparison of various particle mesh routines,” *J. Chem. Phys.* **109**, 7678–7693 (1998).
 - ⁴¹T. Darden, D. York, and L. Pedersen, “Particle mesh ewald: An n-log(n) method for ewald sums in large systems,” *Journal of Chemical Physics* **98**, 10089–10092 (1993).
 - ⁴²U. Essmann, L. Perera, M. L. Berkowitz, T. Darden, H. Lee, and L. G. Pedersen, “A smooth particle mesh ewald method,” *The Journal of chemical physics* **103**, 8577–8593 (1995).
 - ⁴³J. R. Winkler, “Numerical recipes in C: The art of scientific computing, second edition,” *Endeavour* **17**, 201 (1993).
 - ⁴⁴M. Kawata and U. Nagashima, “Particle mesh ewald method for three-dimensional systems with two-dimensional periodicity,” *Chemical Physics Letters* **340**, 165–172 (2001).
 - ⁴⁵W. Gautschi, *Numerical analysis* (Springer Science & Business Media, 2011).
 - ⁴⁶L. Greengard and V. Rokhlin, “A fast algorithm for particle simulations,” *Journal of Computational Physics* **73**, 325–348 (1987).
 - ⁴⁷P. Gibbon and G. Sutmann, “Long-range interactions in many-particle simulation,” *Quantum Simulations of Complex Many-Body Systems: From Theory to Algorithms*, NIC Series , 467–506 (2004).
 - ⁴⁸Z. Deng, C. Chen, X.-G. Li, and S. P. Ong, “An electrostatic spectral neighbor analysis potential for lithium nitride,” *npj Computational Materials* **5**, 1–8 (2019).
 - ⁴⁹V. L. Deringer, M. A. Caro, and G. Csányi, “A general-purpose machine-learning force field for bulk and nanostructured phosphorus,” *Nat Commun* **11**, 5461 (2020).
 - ⁵⁰O. T. Unke, S. Chmiela, M. Gastegger, K. T. Schütt, H. E. Sauceda, and K.-R. Müller, “Spookynet: Learning force fields

- with electronic degrees of freedom and nonlocal effects,” *Nature communications* **12**, 7273 (2021).
- ⁵¹S. P. Niblett, M. Galib, and D. T. Limmer, “Learning intermolecular forces at liquid–vapor interfaces,” *J. Chem. Phys.* **155**, 164101 (2021).
- ⁵²A. Kabylda, J. T. Frank, S. S. Dou, A. Khabibrakhmanov, L. M. Sandonas, O. T. Unke, S. Chmiela, K.-R. Muller, and A. Tkatchenko, “Molecular simulations with a pretrained neural network and universal pairwise force fields,” *chemrxiv preprint* (2024), 10.26434/chemrxiv-2024-bdfr0.
- ⁵³O. T. Unke and M. Meuwly, “Physnet: A neural network for predicting energies, forces, dipole moments, and partial charges,” *Journal of Chemical Theory and Computation* **15**, 3678–3693 (2019), pMID: 31042390, <https://doi.org/10.1021/acs.jctc.9b00181>.
- ⁵⁴A. E. Sifain, N. Lubbers, B. T. Nebgen, J. S. Smith, A. Y. Lokhov, O. Isayev, A. E. Roitberg, K. Barros, and S. Tretiak, “Discovering a transferable charge assignment model using machine learning,” *The Journal of Physical Chemistry Letters* **9**, 4495–4501 (2018), pMID: 30039707, <https://doi.org/10.1021/acs.jpcllett.8b01939>.
- ⁵⁵A. Gao and R. C. Remsing, “Self-consistent determination of long-range electrostatics in neural network potentials,” *Nature Communications* **13**, 1572 (2022).
- ⁵⁶Y. Peng, L. Lin, L. Ying, and L. Zepeda-Núñez, “Efficient long-range convolutions for point clouds,” *Journal of Computational Physics* **473**, 111692 (2023).
- ⁵⁷L. Zhang, H. Wang, M. C. Muniz, A. Z. Panagiotopoulos, R. Car, and W. E, “A deep potential model with long-range electrostatic interactions,” *J. Chem. Phys.* **156**, 124107 (2022).
- ⁵⁸S. Faraji, S. A. Ghasemi, S. Rostami, R. Rasoulkhani, B. Schaefer, S. Goedecker, and M. Amsler, “High accuracy and transferability of a neural network potential through charge equilibration for calcium fluoride,” *Phys. Rev. B* **95**, 104105 (2017).
- ⁵⁹T. W. Ko, J. A. Finkler, S. Goedecker, and J. Behler, “A fourth-generation high-dimensional neural network potential with accurate electrostatics including non-local charge transfer,” *Nat Commun* **12**, 398 (2021).
- ⁶⁰T. W. Ko, J. A. Finkler, S. Goedecker, and J. Behler, “General-Purpose Machine Learning Potentials Capturing Non-local Charge Transfer,” *Acc. Chem. Res.* **54**, 808–817 (2021).
- ⁶¹M. Gubler, J. A. Finkler, M. R. Schäfer, J. Behler, and S. Goedecker, “Accelerating Fourth-Generation Machine Learning Potentials Using Quasi-Linear Scaling Particle Mesh Charge Equilibration,” *J. Chem. Theory Comput.* (2024), 10.1021/acs.jctc.4c00334.
- ⁶²A. Grisafi and M. Ceriotti, “Incorporating long-range physics in atomic-scale machine learning,” *J. Chem. Phys.* **151**, 204105 (2019).
- ⁶³A. Grisafi, J. Nigam, and M. Ceriotti, “Multi-scale approach for the prediction of atomic scale properties,” *Chem. Sci.* **12**, 2078–2090 (2021).
- ⁶⁴K. K. Huguenin-Dumittan, P. Loche, N. Haoran, and M. Ceriotti, “Physics-Inspired Equivariant Descriptors of Nonbonded Interactions,” *J. Phys. Chem. Lett.* , 9612–9618 (2023).
- ⁶⁵S. Chong, F. Bigi, F. Grasselli, P. Loche, M. Kellner, and M. Ceriotti, “Prediction rigidities for data-driven chemistry,” *Faraday Discussions* (2024), 10.1039/D4FD00101J.
- ⁶⁶B. Cheng, “Latent Ewald summation for machine learning of long-range interactions,” (2024), arXiv:2408.15165.
- ⁶⁷C. Faller, M. Kaltak, and G. Kresse, “Density-Based Long-Range Electrostatic Descriptors for Machine Learning Force Fields,” (2024), arXiv:2406.17595.
- ⁶⁸G. Hummer, “The numerical accuracy of truncated ewald sums for periodic systems with long-range coulomb interactions,” *Chemical Physics Letters* **235**, 297–302 (1995).
- ⁶⁹H. G. Petersen, “Accuracy and efficiency of the particle mesh Ewald method,” *The Journal of Chemical Physics* **103**, 3668–3679 (1995).
- ⁷⁰M. Deserno and C. Holm, “How to mesh up Ewald sums. II. An accurate error estimate for the particle–particle–particle-mesh algorithm,” **109**, 7694–7701.
- ⁷¹M. E. Tuckerman, B. J. Berne, and A. Rossi, “Molecular dynamics algorithm for multiple time scales: Systems with disparate masses,” *The Journal of Chemical Physics* **94**, 1465–1469 (1991).
- ⁷²V. Kapil, J. VandeVondele, and M. Ceriotti, “Accurate molecular dynamics and nuclear quantum effects at low cost by multiple steps in real and imaginary time: Using density functional theory to accelerate wavefunction methods,” *The Journal of Chemical Physics* **144**, 054111 (2016).
- ⁷³J. E. House, “Chapter 7 - Ionic bonding and structures of solids,” in *Inorganic Chemistry (Third Edition)*, edited by J. E. House (Academic Press, 2020) pp. 229–274.
- ⁷⁴L. Glasser, “Solid-State Energetics and Electrostatics: Madelung Constants and Madelung Energies,” *Inorg. Chem.* **51**, 2420–2424 (2012).
- ⁷⁵H. J. C. Berendsen, J. R. Grigera, and T. P. Straatsma, “The missing term in effective pair potentials,” *J. Phys. Chem.* **91**, 6269–6271 (1987).
- ⁷⁶G. Fraux, P. Loche, F. Bigi, J. W. Abbott, D. Tisi, A. Goscinski, and M. Ceriotti, “Github repository: Metatensor,” (2024).
- ⁷⁷A. P. Thompson, H. M. Aktulga, R. Berger, D. S. Bolintineanu, W. M. Brown, P. S. Crozier, P. J. in ’t Veld, A. Kohlmeyer, S. G. Moore, T. D. Nguyen, R. Shan, M. J. Stevens, J. Tranchida, C. Trott, and S. J. Plimpton, “LAMMPS - a flexible simulation tool for particle-based materials modeling at the atomic, meso, and continuum scales,” *Computer Physics Communications* **271**, 108171 (2022).
- ⁷⁸G. Bussi, D. Donadio, and M. Parrinello, “Canonical sampling through velocity rescaling,” *The Journal of Chemical Physics* **126**, 014101 (2007).
- ⁷⁹C. Vega and J. L. F. Abascal, “Simulating water with rigid non-polarizable models: A general perspective,” *Phys. Chem. Chem. Phys.* **13**, 19663–19688 (2011).
- ⁸⁰J. Behler, “Four Generations of High-Dimensional Neural Network Potentials,” *Chemical Reviews* **121**, 10037–10072 (2021).
- ⁸¹L. N. Smith and N. Topin, “Super-convergence: Very fast training of neural networks using large learning rates,” in *Artificial intelligence and machine learning for multi-domain operations applications*, Vol. 11006 (SPIE, 2019) pp. 369–386.
- ⁸²G. Fraux, P. Loche, F. Bigi, J. W. Abbott, L. Marsh, S. Klavinek, A. Goscinski, K. K. Huguenin-Dumittan, D. Suman, R. K. Cersonsky, and D. Tisi, “Github repository: featomic,” (2024).
- ⁸³A. Neelov, S. A. Ghasemi, and S. Goedecker, “Particle-particle, particle-scaling function algorithm for electrostatic problems in free boundary conditions,” *The Journal of Chemical Physics* **127**, 024109 (2007).
- ⁸⁴A. Arnold and C. Holm, “MMM1D: A method for calculating electrostatic interactions in one-dimensional periodic geometries,” *The Journal of Chemical Physics* **123**, 144103 (2005).
- ⁸⁵A. Arnold and C. Holm, “MMM2D: A fast and accurate summation method for electrostatic interactions in 2D slab geometries,” *Computer Physics Communications* **148**, 327–348 (2002).
- ⁸⁶V. Ballenegger, A. Arnold, and J. J. Cerdà, “Simulations of non-neutral slab systems with long-range electrostatic interactions in two-dimensional periodic boundary conditions,” *The Journal of Chemical Physics* **131**, 094107 (2009).
- ⁸⁷L. J. V. Ahrens-Iwers and R. H. Meißner, “Constant potential simulations on a mesh,” *The Journal of Chemical Physics* **155**, 104104 (2021).

Fast and flexible long-range models for atomistic machine learning: Supplementary Material

Philip Loche,^{1,2} Kevin K. Huguenin-Dumittan,¹ Melika Honarmand,^{1,2} Qianjun Xu,¹ Egor Rumiantsev,^{1,2} Wei Bin How,^{1,2} Marcel F. Langer,¹ and Michele Ceriotti^{1,2}

¹*Laboratory of Computational Science and Modeling, IMX, École Polytechnique Fédérale de Lausanne, 1015 Lausanne, Switzerland*

²*National Centre for Computational Design and Discovery of Novel Materials (MARVEL), École Polytechnique Fédérale de Lausanne, 1015 Lausanne, Switzerland^{a)}*

CONTENTS

S1. Mathematical Conventions, Notation and Prerequisites	S2
A. Vectors, Norms and Inner Products	S2
B. Lattice and Reciprocal Lattice	S2
C. Unit cells and volumes	S2
D. Fourier Series and Fourier Transforms	S3
E. The Poisson Summation Formula	S4
S2. Derivation of Ewald Summation	S6
A. General Expression using Poisson Summation	S6
B. Self-Term in Ewald Summation	S6
C. Charge Neutralization term in Ewald Sum	S6
D. Treatment of Charge Compensation Term	S8
S3. Relation to LODE and Evolution of Method	S9
A. First Two Mathematical Consequences: From Original to Previous Work	S9
1. First Consequence: Most Features Contain No Long-Range Information	S10
2. Second Consequence: Short-Range Contamination	S10
B. Further Mathematical Consequences: From Last Publication to Current One	S11
1. Third Consequence: Not all coefficients are equal	S11
2. Fourth Consequence: Relations between LODE Features, Potentials and Electric Fields	S12
C. Mathematical Results for General Exponents p	S13
1. Generalized Multipole Expansion	S13
2. Fifth consequence: Results are More Complicated But Similar for General Inverse Power-Law Potential	S13
S4. Tuning the Ewald and PME parameters	S15
S5. Finding the optimal cutoff for benchmarking	S17
S6. GPU Utilization	S18
S7. MD of Water at constant energy and volume	S19
References	S19

^{a)}These two authors contributed equally.

S1. MATHEMATICAL CONVENTIONS, NOTATION AND PREREQUISITES

Many different conventions and notations can be found in the literature for mathematical expressions and concepts. Most relevant to this work are the ones relating to periodic lattices and Fourier transforms. To keep a consistent notation and convention throughout this document, we summarize all definitions in this section. We also briefly summarize some well-known mathematical results about these that are used throughout this document and the implementation.

A. Vectors, Norms and Inner Products

Throughout this document, we shall use the bold-font $\mathbf{r} \in \mathbb{R}^3$ for vectors in Euclidean space, while $r = \|\mathbf{r}\|$ will denote its magnitude computed using the usual 2-norm. Similarly, we will use $\mathbf{k} \in \mathbb{R}^3$ and $k = \|\mathbf{k}\|$ when discussing Fourier transforms, and write either $\mathbf{k} \cdot \mathbf{r}$ or just \mathbf{kr} for the inner product between two vectors.

For an atomic system consisting of $N \in \mathbb{N}$ atoms, we index the atoms by $i, j \in \{1, 2, \dots, N\}$. This is then used to write \mathbf{r}_i for the position vector of atom i , and $r_{ij} = \|\mathbf{r}_j - \mathbf{r}_i\|$ for the distance between atoms i and j .

For the more mathematically inclined readers: \mathbf{r} and \mathbf{k} technically are elements of different vector spaces, both isomorphic to \mathbb{R}^3 , which are duals of each other. In practice, the choice of symbol will unambiguously determine which space is meant.

B. Lattice and Reciprocal Lattice

The lattice Γ spanned by the three linearly independent vectors $\mathbf{a}_1, \mathbf{a}_2, \mathbf{a}_3 \in \mathbb{R}^3$ is defined as

$$\Gamma = \text{span}_{\mathbb{Z}}\{\mathbf{a}_1, \mathbf{a}_2, \mathbf{a}_3\} \quad (\text{S1})$$

$$= \{\mathbf{l} = n_1\mathbf{a}_1 + n_2\mathbf{a}_2 + n_3\mathbf{a}_3 | n_1, n_2, n_3 \in \mathbb{Z}\}. \quad (\text{S2})$$

In practice, these basis vectors will be chosen to specify the periodicity within the cell. We can then define the reciprocal lattice Γ^* by the requirement

$$\Gamma^* = \{\mathbf{k} \in \mathbb{R}^3 | \forall \mathbf{r} \in \Gamma : \mathbf{kr} \in 2\pi\mathbb{Z}\} \quad (\text{S3})$$

which can be shown to be the lattice spanned by the three basis vectors

$$\mathbf{b}_i = 2\pi \frac{\mathbf{a}_j \times \mathbf{a}_k}{\mathbf{a}_i \cdot (\mathbf{a}_j \times \mathbf{a}_k)}, \quad (\text{S4})$$

where (i, j, k) is an even permutation of $(1, 2, 3)$ and \times is the cross-product. We will generally use the symbol $\mathbf{l} \in \Gamma$ to denote an element of the (real space) lattice, i.e. a different symbol from \mathbf{r} , while we use the same symbol $\mathbf{k} \in \Gamma^*$. It should be clear from context which one is meant. In particular, we will write

$$\sum_{\mathbf{k}} \quad (\text{S5})$$

as a shorthand for

$$\sum_{\mathbf{k} \in \Gamma^*} \quad (\text{S6})$$

as the former is likely to be more familiar to be many readers. The summation symbol is emphasizing that \mathbf{k} only runs over the discrete set Γ^* rather than \mathbb{R}^3 .

Note that we do include the factor of 2π directly in the definition of the reciprocal space vectors, since this leads to slightly more compact formulae and also is slightly more convenient for implementations.

C. Unit cells and volumes

In practice, the basis vectors $\mathbf{a}_1, \mathbf{a}_2, \mathbf{a}_3$ introduced in the previous subsection will be used to specify a periodic repetition of atoms. In this case, the volume of the unit cell spanned by the three vectors can be obtained by computing their triple product, and will be denoted by

$$\Omega = \mathbf{a}_1 \cdot (\mathbf{a}_2 \times \mathbf{a}_3). \quad (\text{S7})$$

In order to compute Fourier transforms, it will also be necessary to integrate over such a unit cell. We can thus define the closed set

$$\Omega = \{w_1 \mathbf{a}_1 + w_2 \mathbf{a}_2 + w_3 \mathbf{a}_3 | w_1, w_2, w_3 \in [0, 1]\} \quad (\text{S8})$$

for the unit cell, such that its volume $\Omega = \text{Vol}(\Omega)$.

For the mathematically inclined readers: strictly speaking, it would be more correct to define $\Omega = \mathbb{R}^3/\Gamma$ using a quotient, where Γ is the lattice defined by the basis vectors. With this definition, the periodic structure of the underlying domain becomes more explicit, and it is easy to see that Ω is diffeomorphic to the 3-torus $\mathbb{T}^3 = S^1 \times S^1 \times S^1$ as a smooth manifold.

D. Fourier Series and Fourier Transforms

In this chapter, we shall make extensive use of the Fourier transform in its various forms.

Firstly, consider functions $f : \mathbb{R}^3 \rightarrow \mathbb{C}$ (or more precisely, absolutely integrable functions $f \in L^1(\mathbb{R}^3, \mathbb{C})$). Then, for all $\mathbf{k} \in \mathbb{R}^3$, we define the Fourier transform of f as

$$\hat{f}(\mathbf{k}) = \int_{\mathbb{R}^3} d^3r e^{-i\mathbf{k}\mathbf{r}} f(\mathbf{r}). \quad (\text{S9})$$

The inverse transformation then is given by

$$f(\mathbf{r}) = \frac{1}{(2\pi)^3} \int_{\mathbb{R}^3} d^3k e^{i\mathbf{k}\mathbf{r}} \hat{f}(\mathbf{k}). \quad (\text{S10})$$

The entire factor of $\frac{1}{(2\pi)^3}$ is thus contained in the inverse transform. While this is arguably less elegant from the point of view of symmetry, it will lead to slightly simpler expressions when comparing this to the Fourier series for periodic functions, which will be helpful when discussing the Poisson summation formula.

If the original function f is rotationally symmetric, often written as $f(\mathbf{r}) = f(r)$, then so is its Fourier transform $\hat{f}(\mathbf{k}) = \hat{f}(k)$. By doing the integral in spherical coordinates and integrating with respect to the angular variables (ϕ, θ) , we can obtain the more direct formula relating f to \hat{f} as the one-dimensional integral

$$\hat{f}(k) = 4\pi \int_0^\infty dr r^2 \frac{\sin(kr)}{kr} f(r) \quad (\text{S11})$$

$$= \frac{4\pi}{k} \int_0^\infty dr r \sin(kr) f(r) \quad (\text{S12})$$

and its inverse

$$f(r) = \frac{1}{(2\pi)^3} \frac{4\pi}{r} \int_0^\infty dk k \sin(kr) \hat{f}(k). \quad (\text{S13})$$

In particular, this means that apart from a factor of $\frac{1}{(2\pi)^3}$, the radially symmetric transform is its own inverse. This version of the transform is closely related to the Hankel transform.

So far, we have discussed the Fourier transform of a generic (absolutely integrable) function on \mathbb{R}^3 . We now move on to the Fourier series representation of a periodic function.

Let $f : \mathbb{R}^3 \rightarrow \mathbb{C}$ be a function having the periodicity of a unit cell Ω with its corresponding lattice Γ . More mathematically, this means that for all $\mathbf{r} \in \mathbb{R}^3$ and $\mathbf{l} \in \Gamma$, $f(\mathbf{r} + \mathbf{l}) = f(\mathbf{r})$. The function is clearly specified by just its values in the unit cell Ω .

For any reciprocal space vector $\mathbf{k} \in \Gamma^*$, we then define the Fourier transform (for the periodic case also called Fourier series coefficient) of f as

$$\hat{f}(\mathbf{k}) = \int_{\Omega} d^3r e^{-i\mathbf{k}\mathbf{r}} f(\mathbf{r}). \quad (\text{S14})$$

We can then recover f using the inverse transform

$$f(\mathbf{r}) = \frac{1}{\Omega} \sum_{\mathbf{k} \in \Gamma^*} \hat{f}(\mathbf{k}) e^{i\mathbf{k}\mathbf{r}}. \quad (\text{S15})$$

Note that a common convention is to put the factor of $1/\Omega$ in the (forwards) Fourier transform rather than the inverse. Our convention makes the expressions for the forward transforms for the aperiodic case in Equation S9 and periodic one in Equation S14 more symmetric.

E. The Poisson Summation Formula

The following theorem provides us with an explicit connection between summation in real space and reciprocal space.

Theorem S1.1 (Poisson Summation Formula). *Let $f \in L^1(\mathbb{R}^3, \mathbb{C})$ be an absolutely integrable function, Γ a lattice whose unit cell Ω has a volume Ω and Γ^* its reciprocal lattice. Then, for all $\mathbf{r} \in \mathbb{R}^3$, we get*

$$\sum_{\mathbf{l} \in \Gamma} f(\mathbf{r} + \mathbf{l}) = \frac{1}{\Omega} \sum_{\mathbf{k} \in \Gamma^*} \hat{f}(\mathbf{k}) e^{i\mathbf{k}\mathbf{r}}. \quad (\text{S16})$$

In other words, a sum of the values of f over a lattice Γ can be expressed as a sum over reciprocal space vectors.

While this is a standard result in mathematical methods, it is so important to our work that we provide a short proof for the convenience of the reader. There is no originality in the proof, and this is merely to make this document more self-contained.

Proof. Let $F(\mathbf{r}) = \sum_{\mathbf{l} \in \Gamma} f(\mathbf{r} + \mathbf{l})$ be the left-hand side. We will first show that F is a periodic function with respect to the lattice Γ . From the inversion of Fourier transforms for periodic functions, this then means that we can write F using its Fourier series coefficients $\hat{F}(\mathbf{k})$ as

$$F(\mathbf{r}) = \frac{1}{\Omega} \sum_{\mathbf{k} \in \Gamma^*} \hat{F}(\mathbf{k}) e^{i\mathbf{k}\mathbf{r}}. \quad (\text{S17})$$

Comparing this with the theorem, we can see that all we need to do is to show that $\hat{F}(\mathbf{k}) = \hat{f}(\mathbf{k})$ for all $\mathbf{k} \in \Gamma^*$.

Starting with the periodicity of F , this comes from the fact that for two lattice vectors $\mathbf{l}, \mathbf{l}' \in \Gamma$, their sum is still just a lattice vector $\mathbf{l}'' = \mathbf{l} + \mathbf{l}' \in \Gamma$. A sum over all $\mathbf{l}' \in \Gamma$ is equivalent to a sum over all $\mathbf{l}'' = \mathbf{l} + \mathbf{l}'$, since we are effectively just shifting the origin of the lattice by \mathbf{l} . Thus,

$$F(\mathbf{r} + \mathbf{l}) = \sum_{\mathbf{l}' \in \Gamma} f(\mathbf{r} + \mathbf{l} + \mathbf{l}') \quad (\text{S18})$$

$$= \sum_{\mathbf{l}'' \in \Gamma} f(\mathbf{r} + \mathbf{l}'') \quad (\text{S19})$$

$$= F(\mathbf{r}). \quad (\text{S20})$$

We can thus compute the Fourier transform of F (the variant for periodic functions, also called Fourier series) directly from the definition in Equation S14. For $\mathbf{k} \in \Gamma^*$, we get

$$\hat{F}(\mathbf{k}) = \int_{\Omega} d^3r e^{-i\mathbf{k}\mathbf{r}} F(\mathbf{r}) \quad (\text{S21})$$

$$= \int_{\Omega} d^3r e^{-i\mathbf{k}\mathbf{r}} \sum_{\mathbf{l} \in \Gamma} f(\mathbf{r} + \mathbf{l}) \quad (\text{S22})$$

$$\stackrel{\text{Fubini}}{=} \sum_{\mathbf{l} \in \Gamma} \int_{\Omega} d^3r e^{-i\mathbf{k}\mathbf{r}} f(\mathbf{r} + \mathbf{l}) \quad (\text{S23})$$

$$\stackrel{\mathbf{k}\mathbf{l}=2\pi\mathbf{n}}{=} \sum_{\mathbf{l} \in \Gamma} \int_{\Omega} d^3r e^{-i\mathbf{k}(\mathbf{r}+\mathbf{l})} f(\mathbf{r} + \mathbf{l}) \quad (\text{S24})$$

$$\stackrel{\mathbf{r}'=\mathbf{r}+\mathbf{l}}{=} \int_{\mathbb{R}^3} d^3r' e^{-i\mathbf{k}\mathbf{r}'} f(\mathbf{r}') \quad (\text{S25})$$

$$= \hat{f}(\mathbf{k}). \quad (\text{S26})$$

This shows that the Fourier series coefficients $\hat{F}(\mathbf{k})$ of the periodic function F are actually identical to the Fourier transform of the (in general, aperiodic) function f . The only key difference is that $\hat{f}(\mathbf{k})$ is defined for all $\mathbf{k} \in \mathbb{R}^3$, while $\hat{F}(\mathbf{k})$ only is defined for $\mathbf{k} \in \Gamma^*$. Thus, \hat{F} is merely the restriction of \hat{f} onto the reciprocal lattice Γ^* .

We can now use the inverse transform for F , which allows us to write

$$F(\mathbf{r}) = \frac{1}{\Omega} \sum_{\mathbf{k} \in \Gamma^*} \hat{F}(\mathbf{k}) e^{i\mathbf{k}\mathbf{r}}. \quad (\text{S27})$$

But since $\hat{F}(\mathbf{k}) = \hat{f}(\mathbf{k})$, this leads to

$$F(\mathbf{r}) = \frac{1}{\Omega} \sum_{\mathbf{k} \in \Gamma^*} \hat{f}(\mathbf{k}) e^{i\mathbf{k}\mathbf{r}}. \quad (\text{S28})$$

Remembering that we had defined $F(\mathbf{r}) = \sum_{\mathbf{l}} f(\mathbf{r} + \mathbf{l})$, this concludes the theorem. \square

S2. DERIVATION OF EWALD SUMMATION

A. General Expression using Poisson Summation

In this section, we derive the general decomposition of the potential into its four terms in the Ewald summation. For an explanation of the notation and terminology related to unit cells, periodic lattices and Fourier transforms, please refer to the previous section.

The results in this section are already known in the literature. The purpose of this section is to make this paper self-contained, and to include derivations of all results using a consistent notation that we also use in the main text.

B. Self-Term in Ewald Summation

The self-term in Ewald summation can be obtained by computing the limit

$$v_{\text{self}} = \lim_{r \rightarrow 0} v_{\text{LR}}(r). \quad (\text{S29})$$

To evaluate this, we can use the Taylor series expansion of the lower incomplete Gamma function, which can be derived directly from its definition and using Fubini's theorem to interchange the order of summation and integration for $a > 0$:

$$\gamma(a, x) = \int_0^x dt t^{a-1} e^{-t} \quad (\text{S30})$$

$$= \int_0^x dt t^{a-1} \sum_{n=0}^{\infty} \frac{(-1)^n}{n!} t^n \quad (\text{S31})$$

$$= \sum_{n=0}^{\infty} \frac{(-1)^n}{n!} \int_0^x dt t^{n+a-1} \quad (\text{S32})$$

$$= \sum_{n=0}^{\infty} \frac{(-1)^n}{n!} \frac{1}{a+n} x^{a+n} \quad (\text{S33})$$

$$= \frac{1}{a} x^a + \mathcal{O}(x^{a+1}). \quad (\text{S34})$$

Using this, we obtain

$$v_{\text{self}} = \lim_{r \rightarrow 0} \frac{1}{\Gamma\left(\frac{p}{2}\right)} \frac{\gamma\left(\frac{p}{2}, \frac{r^2}{2\sigma^2}\right)}{r^p} \quad (\text{S35})$$

$$= \frac{1}{\Gamma\left(\frac{p}{2}\right)} \frac{2}{p} (2\sigma^2)^{-\frac{p}{2}} \quad (\text{S36})$$

$$= \frac{1}{\Gamma\left(\frac{p}{2} + 1\right) (2\sigma^2)^{\frac{p}{2}}} \quad (\text{S37})$$

C. Charge Neutralization term in Ewald Sum

The correction term to enforce charge neutrality arises from the interaction of the particles with a homogeneous background charge density that is used to neutralize the system.

For this, consider the Green's function $G(\mathbf{r}, \mathbf{r}')$ describing the potential at position \mathbf{r} , assuming the presence of a particle at \mathbf{r}' with weight (or charge) $q = 1$, including its periodic images and a homogeneous background with total

charge $-q$ per unit cell to fulfill charge neutrality. Then,

$$G(\mathbf{r}, \mathbf{r}') = \sum_{\mathbf{l} \in \Gamma} v(\mathbf{r} - \mathbf{r}' + \mathbf{l}) - \frac{1}{\Omega} \int_{\mathbb{R}^3} d\mathbf{r}' v(\mathbf{r}') \quad (\text{S38})$$

$$= \sum_{\mathbf{l} \in \Gamma} v_{\text{SR}}(\mathbf{r} - \mathbf{r}' + \mathbf{l}) + \sum_{\mathbf{l} \in \Gamma} v_{\text{LR}}(\mathbf{r} - \mathbf{r}' + \mathbf{l}) - \frac{1}{\Omega} \int_{\mathbb{R}^3} d\mathbf{r}' v(\mathbf{r}') \quad (\text{S39})$$

$$= \sum_{\mathbf{l} \in \Gamma} v_{\text{SR}}(\mathbf{r} - \mathbf{r}' + \mathbf{l}) + \frac{1}{\Omega} \sum_{\mathbf{k} \neq 0} \hat{v}_{\text{LR}}(\mathbf{k}) e^{i\mathbf{k}(\mathbf{r} - \mathbf{r}')} \quad (\text{S40})$$

We now take the integral of this expression over the entire unit cell to average over the positions of the particle, which leads to

$$v_{\text{charge}} = \frac{1}{2} \frac{q}{\Omega} \int_{\Omega} d\mathbf{r}' G(\mathbf{r}, \mathbf{r}') \quad (\text{S41})$$

Bringing the global factor of q/Ω to the other side, we get

$$\frac{\Omega}{q} v_{\text{charge}} = \frac{1}{2} \int_{\Omega} d\mathbf{r}' \sum_{\mathbf{l} \in \Gamma} v_{\text{SR}}(\mathbf{r} - \mathbf{r}' + \mathbf{l}) + \frac{1}{\Omega} \int_{\Omega} d\mathbf{r}' \sum_{\mathbf{k} \neq 0} \hat{v}_{\text{LR}}(\mathbf{k}) e^{i\mathbf{k}(\mathbf{r} - \mathbf{r}')} \quad (\text{S42})$$

In the first term, \mathbf{r}' runs over a single cell, to which we add the periodic shifts \mathbf{l} . This term therefore simply corresponds to the integral over the entire space \mathbb{R}^3 . For the second term, using the fact that $\mathbf{k} \in \Gamma^*$ are reciprocal space lattice vectors, we can evaluate the sum using

$$\frac{1}{\Omega} \int_{\Omega} d\mathbf{r}' e^{i\mathbf{k}\mathbf{r}'} = \delta_{0,\mathbf{k}} \quad (\text{S43})$$

to see that this term vanishes. Hence, the core calculation of the charge correction term has been reduced to the computation of

$$v_{\text{charge}} = \frac{1}{2} \int_{\mathbb{R}^3} d\mathbf{r}' v_{\text{SR}}(r') \quad (\text{S44})$$

$$= 2\pi \int_0^{\infty} dr r^2 v_{\text{SR}}(r), \quad (\text{S45})$$

where we used spherical symmetry in the last step.

While we could directly start computing this for the general case, it is instructive to first study the behavior at the two bounds of the integral, i.e. what happens in the limits as $r \rightarrow 0$ and $r \rightarrow \infty$. Firstly, since $v_{\text{SR}}(r)$ was explicitly constructed to decay quickly as $r \rightarrow \infty$, the upper bound of integration does not cause any problems. On the other hand, we know that v_{SR} contains the singularity of the bare $1/r^p$ potential as $r \rightarrow 0$. To estimate the lower bound of integration, we can thus study the simplified integral

$$\int_0^R dr r^2 \frac{1}{r^p} = \int_0^R dr r^{2-p}, \quad (\text{S46})$$

$$= \begin{cases} \frac{1}{3-p} r^{3-p} \Big|_0^R & p \neq 3 \\ \log p \Big|_0^R & p = 3 \end{cases} \quad (\text{S47})$$

$$= \lim_{\epsilon \rightarrow 0} \begin{cases} \frac{1}{3-p} R^{3-p} - \epsilon^{3-p} & p < 3 \\ \log R - \log \epsilon & p = 3 \\ -\frac{1}{p-3} \frac{1}{R^{p-3}} + \frac{1}{p-3} \frac{1}{\epsilon^{p-3}} & p > 3 \end{cases} \quad (\text{S48})$$

$$= \begin{cases} \frac{1}{3-p} R^{3-p} & p < 3 \\ +\infty & p = 3 \\ +\infty & p > 3 \end{cases} \quad (\text{S49})$$

Note that for the third case where $p > 3$, we wrote all results in terms of $p - 3 > 0$ instead of $3 - p < 0$ to make all prefactors and exponents positive. These results clearly show that due to the strong singularity at zero distance, the charge correction term due to a homogeneous background can only be evaluated for $p < 3$.

Now focusing only on $p < 3$ where the full integral for v_{charge} is well-defined, we obtain

$$v_{\text{charge}} = 2\pi \int_0^\infty dr r^2 v_{\text{SR}}(r) \quad (\text{S50})$$

$$= \frac{2\pi}{\Gamma\left(\frac{p}{2}\right)} \int_0^\infty dr r^{2-p} \Gamma\left(\frac{p}{2}, \frac{r^2}{2\sigma^2}\right) \quad (\text{S51})$$

$$= \frac{2\pi}{\Gamma\left(\frac{p}{2}\right)} \int_0^\infty dr r^{2-p} \int_{\frac{r^2}{2\sigma^2}}^\infty dt t^{\frac{p}{2}-1} e^{-t} \quad (\text{S52})$$

Using Fubini's theorem to swap the order of the two integrals and appropriately adjusting the integral boundaries (which is allowed for $p < 3$ since the integrand can be estimated by a power law), we obtain

$$v_{\text{charge}} = \frac{2\pi}{\Gamma\left(\frac{p}{2}\right)} \int_0^\infty dt t^{\frac{p}{2}-1} e^{-t} \int_0^{\sqrt{2\sigma^2 t}} dr r^{2-p} \quad (\text{S53})$$

$$= \frac{2\pi}{\Gamma\left(\frac{p}{2}\right)} \int_0^\infty dt t^{\frac{p}{2}-1} e^{-t} \frac{1}{3-p} (2\sigma^2 t)^{\frac{3-p}{2}} \quad (\text{S54})$$

$$= \frac{2\pi (2\sigma^2)^{\frac{3-p}{2}}}{(3-p)\Gamma\left(\frac{p}{2}\right)} \int_0^\infty dt t^{\frac{1}{2}} e^{-t} \quad (\text{S55})$$

$$= \frac{\pi^{\frac{3}{2}} (2\sigma^2)^{\frac{3-p}{2}}}{(3-p)\Gamma\left(\frac{p}{2}\right)}. \quad (\text{S56})$$

For the two special cases of $p = 1$, this reduces to

$$v_{\text{charge}}^{p=1} = \pi\sigma^2 \quad (\text{S57})$$

and for $p = 2$ to

$$v_{\text{charge}}^{p=2} = \sqrt{2\pi^3}\sigma. \quad (\text{S58})$$

D. Treatment of Charge Compensation Term

Summarizing the results on the compensation term and the subtlety regarding the critical exponent of $p = 3$:

1. For $p \leq 3$, the sums used to compute the potential are divergent if the cell is not charge neutral, thus requiring the addition of a homogeneous charge density of opposite total charge to ensure a neutral cell. The potential of some particle i then consists of contributions from the remaining particles (including periodic images), and a second term $V_{i,\text{charge}}$ arising from the interaction of the particle with the homogeneous background. Using a compensating background for $p > 3$ is not necessary, and as we show below, it is in fact not possible, as such a term would diverge.
2. This additional interaction $V_{i,\text{charge}}$ has been computed explicitly in the previous subsection, and can be seen to be finite for $p < 3$ and divergent for $p \geq 3$. Thus, one approach is to use a compensating background for $p < 3$ and to properly take into account the additional interaction with the background charge using $V_{i,\text{charge}}$, while not to use any background at all for $p > 3$, and hence also $V_{i,\text{charge}}$.
3. For the critical case $p = 3$, charge neutrality does need to be enforced, but due to the divergence of the interaction between a potential compensating background, it is not possible to account for this. We thus set $V_{i,\text{charge}} = 0$, which essentially means that for this special case, we are not fully taking into account the interaction between the background and the particles.
4. To be more consistent and ensure continuity of the potentials as the exponent p is varied, it would be an option to also set $V_{i,\text{charge}} = 0$ for $p < 3$. While this is a possibility, we decided against this as for the most important case of the Coulomb potential, it is common to include this term. We have therefore prioritized consistency with other Ewald implementations for $p = 1$. It should be easy for power users to change this to any other desired convention.

S3. RELATION TO LODE AND EVOLUTION OF METHOD

We now discuss in some detail the relation between this work and some of our previous work for long-range ML, in which we have introduced the Long-Distance Equivariant (LODE) descriptors[?] and extensions thereof[?]. While the framework presented in this work does also support LODE, we recommend in most cases to use the simpler (exterior) potential features. As we will now show, the majority of the long-ranged information of a system is contained in these features. For more complicated cases, however, there might be benefits to using the full LODE features.

The central tool that has driven these developments is a mathematical theorem called multipole expansion, which is discussed in detail in the supporting information of our previous work[?].

The first half of this section discusses some of the key ideas that led from the original formulation[?] to previous work published in 2023[?]. The second half then discusses the more recent developments that led to this work.

A. First Two Mathematical Consequences: From Original to Previous Work

We begin by discussing some of the inefficiencies in the original formulation of LODE[?], which have already been addressed in a previous publication[?]. We provide this background because our newer developments are continuations of these improvements, and also to provide a more transparent description of why we decided to seemingly change direction.

The LODE features (assuming a single chemical species for simplicity) are parametrized by three indices (n, ℓ, m) , $n = 0, 1, \dots, n_{\max} - 1$, $\ell = 0, 1, \dots, \ell_{\max}$ and for each ℓ , m takes the usual $(2\ell + 1)$ distinct values $m \in \{-\ell, -\ell + 1, \dots, \ell\}$. Hence, for fixed ℓ_{\max}, n_{\max} , the total number of LODE features is given by

$$n_{\max} \cdot (\ell_{\max} + 1)^2. \tag{S59}$$

This number is directly proportional to the computational cost that is required to generate the features – although when using a reciprocal-space implementation there is a large constant overhead associated with the global Fourier transform operations that might be dominant over the cost of computing individual features. If there are N_a distinct chemical species in the system, this number is further multiplied by N_a . Hence, to reduce the computational cost of the already expensive long-range part, it is essential to make sure that the relevant long-range information is concentrated in as few coefficients as possible. It was shown previously that the original method proposed in[?] is not doing this efficiently.

To guide the following discussion, we will use $n_{\max} = 6$ and $\ell_{\max} = 4$ as an example, for which we obtain $n_{\max} \cdot (\ell_{\max} + 1)^2 = 150$ features. A visual representation of all those features is presented in Figure S1. Each of the 150 blue boxes corresponds to one feature, i.e. one set of possible values (n, ℓ, m) , ordered according to the radial index n in the horizontal and angular index ℓ in the vertical direction. The number of boxes is proportional to the computational cost of evaluating the features, and we will now examine how much long-range information is actually contained in these.

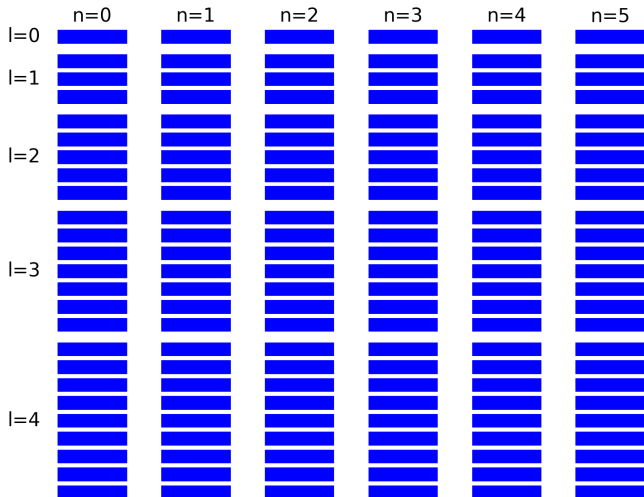


Figure S1. Visualization of features for $n_{\max} = 6$ and $\ell_{\max} = 4$ for the Coulomb potential. Each of the $n_{\max} \cdot (\ell_{\max} + 1)^2 = 150$ blue blocks corresponds to one feature that is computed when working with the LODE descriptor. Thus, the computational cost to get the LODE features is directly proportional to this number.

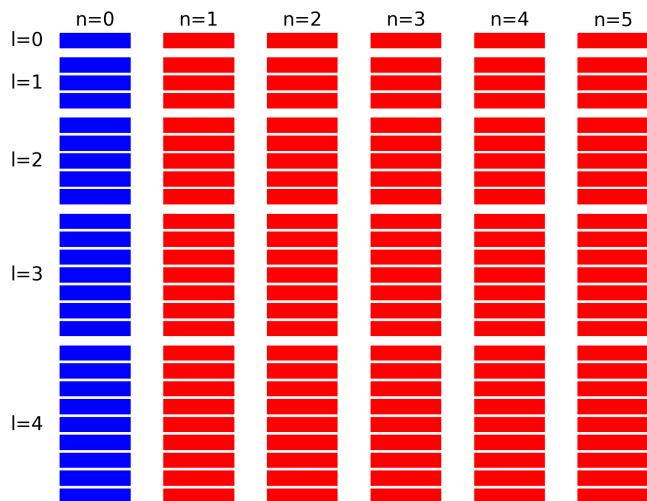


Figure S2. Visualization of LODE features for $n_{\max} = 6$ and $\ell_{\max} = 4$ for the Coulomb potential. The color corresponds to the amount of long-range information in the coefficient, with red meaning exactly zero information. This visualization shows that most features apart from the column with $n = 0$ are completely useless: they do not contain any long-range information.

1. First Consequence: Most Features Contain No Long-Range Information

We begin our discussion with the Coulomb potential. The key mathematical tool for this entire discussion will be the multipole expansion theorem, which is discussed in detail in the supporting information of⁷. The discussion here will however be much more high-level, meaning that it is not necessary to understand the mathematical details of the theorem. It is important to note, however, that the results have been derived using open boundary conditions (for a charge density present in the entire space \mathbb{R}^3 decaying sufficiently quickly to be more precise), and not for periodic boundary conditions.

The first consequence of the multipole expansion theorem is that the entire long-range information can be condensed into a single radial channel, e.g. into the coefficients where $n = 0$.

This is visually represented in Figure S2 for our working example: out of the 150 coefficients that we needed to compute, it turns out that only 25 contain long-range information, while the remaining 125 or $\frac{5}{6} \approx 83\%$ in fact contain no long-range information at all! What this means in more practical terms is that if we keep the position of all atoms within a cutoff, but move the atoms outside of the cutoff, all features for $n > 0$ will be invariant under this operation. The coefficients for $n > 0$ therefore only depend on the position of the interior atoms.

Since the computational cost to evaluate the LODE features (after performing the reciprocal-space part of the algorithm) is proportional to the number of coefficients, we are essentially wasting $\frac{5}{6} \approx 83\%$ of computational cost to compute some numbers that are pure short-range descriptors, the only difference being that the implementation is using a much more sophisticated and expensive algorithm. Given that long-range features are usually combined with another implementation that provides short-range descriptors, we are essentially just wasting computational effort. For a general value of n_{\max} , the fraction of wasted computational effort is $1 - \frac{1}{n_{\max}}$. Note that this discussion only applies to the Coulomb potential, while the more general case of a power-law potential is discussed later.

This provides us with a simple and immediate optimization: we can simply stop computing features for $n > 0$, and only focus on $n = 0$. This leads to an improvement of the computational cost by a factor of typical values of n_{\max} , which is on the order of $6 \sim 12$ for many applications, and hence about an order of magnitude.

2. Second Consequence: Short-Range Contamination

The second key deficit of the original LODE formulation, as well as many alternative approaches to long-range ML as we discussed in the main text, is the fact that even the slowly-decaying Coulomb potential is primarily determined by short-range contributions from immediate neighbors (see also fig. 2 in the main text). While this is fine if our goal is to learn an actual Coulomb potential, this makes the methods less suitable for more general long-range ML.

What this means for our working example of LODE with $n_{\max} = 6$ and $\ell_{\max} = 4$ is visually illustrated in S3. We had already identified the column for $n = 0$ as the only one containing long-range information, but even this is mostly just short-range information with a tiny bit of long-range on top. This means that in the original formulation (and implementation) of LODE⁷, a user would have spent a large computational cost to evaluate 150 features, 125 of which contain exactly zero long-range information, while the remaining 25 are also mostly short-range information.

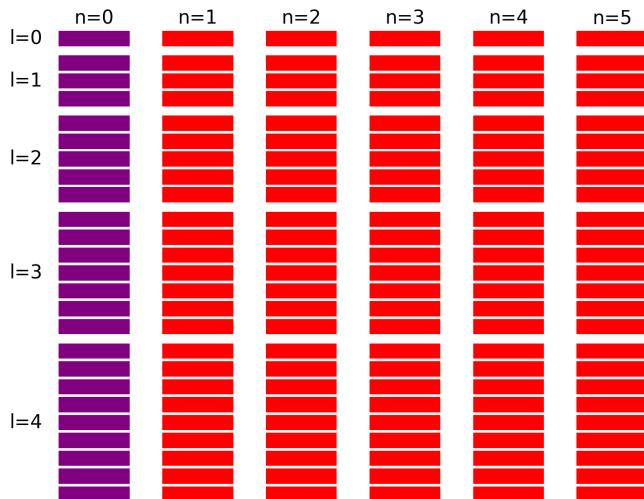


Figure S3. Visualization of features for $n_{\max} = 6$ and $\ell_{\max} = 4$ for the Coulomb potential. The color corresponds to the amount of long-range information in the coefficient, with red meaning exactly zero information, and purple meaning that the information is mostly short-ranged, with a tiny hint of long-range. We can therefore see that out of the 150 coefficients, essentially all of them are completely useless for any realistic task in long-range ML.

While a sufficiently complex neural network might in principle be able to extract some long-range contributions from the 25 features, this signal is hidden behind the much larger short-range contributions that act as noise, making it unrealistic for this to happen in realistic datasets.

As we also recommend in the main text, short-ranged models today are quite mature, and much more efficient at capturing short-range information. Furthermore, it is also this short-range part that contains the dominant part of interactions, with long-range parts being corrections. This is why we always recommend to use long-range features in combination with a short-range ML part. In particular, this means that the $n = 0$ components of the LODE features, which are mostly short-ranged with a tiny fraction of long-range information, are unlikely to improve model performance by any significant extent.

The only exceptions to this general guideline are toy systems that have been constructed specifically to be challenging for short-range models. The original papers mostly discussed such systems, but did not include more realistic target materials, which made it harder to realize that LODE was essentially just computing short-range features in a very expensive manner.

The solution to this problem is the subtraction of the interior contributions. This makes the potential “unphysical”, but leads to descriptors that only contain long-range information. This is analogous to the “purified” long-range descriptors, also called exterior potential features (EPFs) in this work.

Both of these issues have already been addressed in our previous work[?], and the suggested solutions been implemented.

B. Further Mathematical Consequences: From Last Publication to Current One

The two mathematical consequences and possible optimizations obtained from the multipole expansion theorem discussed so far had already been addressed in our last publication[?]. We now discuss further mathematical consequences from the theorem, which strongly influenced the direction taken in this work.

1. Third Consequence: Not all coefficients are equal

So far, we have argued that only the LODE coefficients for $n = 0$ contain long-range information (consequence 1) and that even extracting this information requires a purification process (consequence 2, also discussed in the main text). At the end of these steps, we still have to compute for each pair (ℓ, m) , where $\ell = 0, 1, \dots, \ell_{\max}$ and $m \in \{-\ell, \dots, \ell\}$. The third consequence from the multipole expansion theorem is the fact that the “amount” of long-range information in each of those coefficients depends on ℓ . Note that the discussion here is still restricted to the Coulomb potential, with the general case delegated to the last subsection.

Stated slightly more mathematically, the third consequence states that in a LODE coefficient corresponding to the

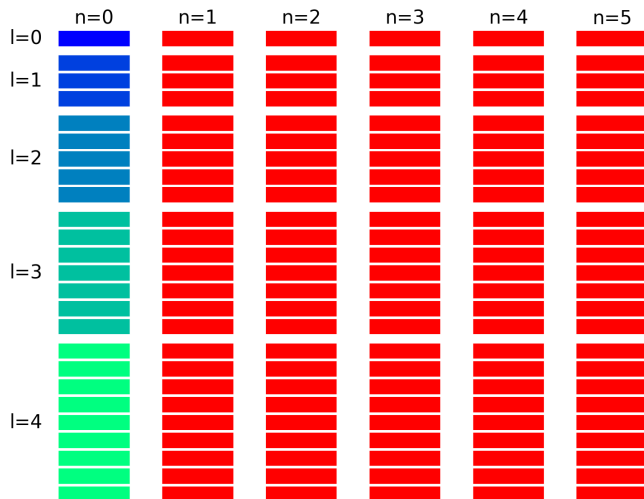


Figure S4. Visualization of LODE features and $n_{\max} = 6$ and $\ell_{\max} = 4$. The color of the block shows the amount of long-range information in the coefficient: the bluer the color, the more information there is. We can see that most long-range information is contained in $n = 0$ and $l = 0, 1, 2$.

indices (ℓ, m) , the contribution of an atom at a distance r is proportional to

$$\frac{1}{r^{1+\ell}}. \quad (\text{S60})$$

i.e. decaying faster for larger indices ℓ . In particular, this reduces to $1/r$ for $\ell = 0$, which is not surprising given that we are working with the Coulomb potential to begin with. For $\ell = 1$, the contribution of an atom decays as $1/r^2$. This is the same decay as the electric field, and we will shortly explain that this is not a coincidence (the three coefficients for $\ell = 1$ basically are the components of the electric field). More generally, as we keep making ℓ large, the atomic contributions start to decay faster and faster. In particular, using a large angular index of $\ell = 8$ would lead to contributions decaying as $1/r^9$, which can hardly be characterized as long-range.

Figure S4 contains a visual representation of this fact. The bluer the color, the more long-ranged the information in the coefficients. This tells us that if the goal is to have a multi-scale model that combines short- and long-range features, it will suffice to only use LODE coefficients of small ℓ , e.g. only $\ell = 0, 1, 2$.

2. Fourth Consequence: Relations between LODE Features, Potentials and Electric Fields

The fourth consequence from the multipole expansion theorem is that in a certain limit (namely the one in which the cutoff radius $r_{\text{cut}} \rightarrow 0$), the LODE coefficient for $\ell = 0$ (and hence $m = 0$) becomes equal to the electrostatic potential at the position of the center atom, while the three LODE coefficients for $\ell = 1$ (and hence $m = \{-1, 0, 1\}$) become equal to the three components of the electric field at the position of the center atom. Note that to be more precise, both “equalities” are only true up to a global prefactor which can be computed analytically, and depends on the choice of LODE basis functions.

This fourth consequence is consistent with our previous observation, that the contribution of an atom at a distance r decays as $1/r^{1+\ell}$, as this leads to $1/r$ for $\ell = 0$ and $1/r^2$ for $\ell = 1$. Note that the electric field is just the first derivative (or gradient to be more precise) of the potential. Focusing just on the radial dependence, $1/r^2$ is the first derivative of $1/r$ with respect to r up to a global prefactor of (-1) .

More generally, the ℓ -th derivative of $1/r$ is $1/r^{1+\ell}$ up to a prefactor, which is precisely the contribution of an atom to a LODE coefficient with index ℓ . We might hence guess that more generally, the LODE components for some ℓ are related to the ℓ -th derivatives of the potential. This guess turns out to be correct, and can be proven using the connection between the spherical and Cartesian versions of the multipole expansion.

Thus, if implemented using an autodifferentiable framework such as *PyTorch* or *JAX*, one can in principle obtain all LODE coefficients just from the EPFs via suitable differentiation.

In other words, it suffices to implement the EPFs (the $\ell = 0$ part), which will automatically provide us with the components for $\ell = 1$ by taking a single differentiation step, $\ell = 2$ by using second derivatives etc. This procedure clearly becomes less and less efficient for larger ℓ , but shows that in principle, our framework is fully able to generate the LODE features without too much extra effort. The main text also discusses some additional capabilities that have been added to also compute the features for higher angular indices ℓ efficiently.

Despite of this possibility, we do not recommend to use higher- ℓ coefficients too extensively. This is due to the previous observation that the larger ℓ becomes, the faster the contributions of the far-away atoms decay. This is why in this work, we suggest alternative methods to extract long-range information more efficiently: by modifying the particle weights (or charges) q_i and the interaction exponent p . The next subsection discusses how some of the results discussed so far change when moving to a more general exponent p .

C. Mathematical Results for General Exponents p

The results so far have exclusively been about the Coulomb potential, which is the most important long-range interaction. Both the LODE features and the EPFs introduced in this work can however easily be generalized to arbitrary $1/r^p$ inverse power-law potentials with $p > 0$ being a positive real number.

As discussed extensively in the supporting information of our previous work⁷, the multipole expansion theorem for this general case is quite different from the Coulomb potential, which is the special case for $p = 1$. It might at first seem surprising that among all positive reals, the Coulomb potential only is very different. We thus explain this first in the next subsection. Readers only interested in the consequences for ML models can skip directly to the final part.

1. Generalized Multipole Expansion

The special nature of the Coulomb potential $v(r) = 1/r$ arises from the fact that it is a solution to the Laplace equation

$$\Delta v = \nabla^2 v = 0 \tag{S61}$$

for $r \neq 0$, where $\Delta = \nabla^2$ is the Laplace-operator. In fact, it is the unique spherically symmetric solution to this equation apart from the constant function! This defining property of the Coulomb potential, perhaps surprisingly, has a dramatic impact on its multipole expansion.

Remembering the definition of the Laplace operator, this means that a certain linear combination of second derivatives of v vanishes. If we perform a Taylor expansion (in three dimensions) of a generic smooth function v , the quadratic term consists of 6 independent terms proportional to $x^2, y^2, z^2, xy, xz, yz$ respectively (since $xy = yx$ commute, as do the derivatives). The prefactors of these terms are precisely the six second derivatives of the target function with respect to two of the three variables. If a function v is a solution to the Laplace equation, however, this means that a linear combination of these six second derivatives is zero, and hence that only five of the derivatives are actually independent. This is why for the Coulomb potential, the contributions with $\ell = 2$ decaying as $1/r^{1+\ell} = 1/r^3$ only contain five terms: $m \in \{-2, -1, 0, 1, 2\}$. The pattern of vanishing derivatives propagates to higher-order derivatives, which means that for the ℓ -th derivatives, only $2\ell + 1$ are independent. This is what makes the Coulomb potential so special when it comes to its Taylor expansion.

For a more generic function, i.e. a function that is not a solution of the Laplace equation, there are no such cancellations, and in general at order ℓ , there are

$$\binom{\ell+2}{2} = \frac{(\ell+2)(\ell+1)}{2} \sim \ell^2 \tag{S62}$$

independent terms in its Taylor expansion. This Taylor expansion is also called ‘‘Cartesian multipole expansion’’, as all the terms of ℓ -th derivatives decay as $1/r^{1+\ell}$ (with some angular dependence), just as for the usual or ‘‘spherical’’ multipole expansion.

So far, we have explained how the Taylor or Cartesian multipole expansion of a generic $1/r^p$ potential contains a lot more terms than $1/r$. The final step to fully make the connection to the LODE coefficients is to connect this Cartesian multipole expansion to the usual ‘‘spherical’’ multipole expansion. This last step simply requires the realization that a spherical harmonic function Y_ℓ^m is, up to a factor of r^ℓ , just a polynomial of degree ℓ in the Cartesian coordinates (x, y, z) . Hence, going from the Cartesian coordinates to spherical harmonics is simply a linear change of basis, which shows that both the Cartesian and spherical multipole expansions are equivalent term-by-term up to a change of basis. The more explicit statements are discussed in the next subsection.

2. Fifth consequence: Results are More Complicated But Similar for General Inverse Power-Law Potential

For LODE features generated from a general $1/r^p$ inverse power-law potential with $p \neq 1$, the information content in the LODE coefficients behaves differently from the Coulomb potential. The generalized multipole expansion discussed

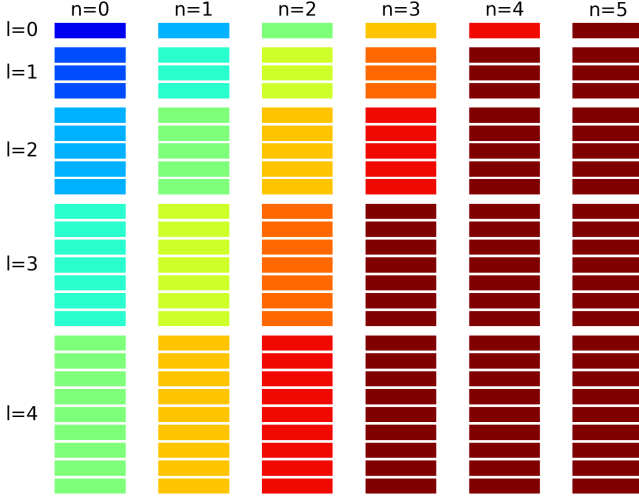


Figure S5. Visualization of LODE features and their long-range information content for $n_{\max} = 6$ and $\ell_{\max} = 4$ for a general $1/r^p$ inverse power-law potential. The color of the block corresponds to the amount of long-range information in the coefficient. We see that the long-range information decreases for large n and ℓ .

in the supporting information in our previous work[?] shows that it is not possible to condense the entire long-range information into $n = 0$, and that all values of n are relevant. Hence, there are now relevant LODE coefficients for all values of the indices (ℓ, m, n) rather than just (ℓ, m) .

For a given coefficient, the contribution of an atom at a distance of r from the center then decays as

$$\frac{1}{r^{p+\ell+2n}}. \quad (\text{S63})$$

This shows more directly that all radial channels n are important, but also that the decay is much faster for large n . Hence, the general trends are still similar to the Coulomb potential: The majority of the long-range information is contained in the coefficients with $n = 0$ and small values of ℓ such as $\ell = 0, 1, 2$. The only difference is that now, also the coefficients with $n = 1, 2$ contain some long-range information. This is visualized in Figure S5.

The relation between the potential (or EPFs) and the analogue of the electric field are the same as for the Coulomb potential. The LODE coefficient for $n = 0$ and $\ell = 0$ still corresponds to the potential (or EPF) at the location of the center atom. Furthermore, the three “generalized electric field” coefficients with $n = 0$ and $\ell = 1$ (and hence $m \in \{-1, 0, 1\}$) by taking the gradient of the coefficient with $n = 0$ and $\ell = 0$.

Despite of this more complicated nature, these facts and the fast decay with respect to n means that the conclusions are mostly similar to the Coulomb potential. This is why instead of building expensive LODE features by using multiple values of ℓ and n , we suggest to just use the potential itself (which essentially corresponds to LODE with $n = \ell = m = 0$) with different charges and the option to add gradients (essentially adding the coefficients for $\ell = 1$) either using the full or exterior variant.

S4. TUNING THE EWALD AND PME PARAMETERS

In the following, we discuss the procedure we implement to tune the optimal parameters, by minimizing the absolute force error estimation. We define the total force error as

$$\Delta F = \sqrt{\Delta F_{\text{SR}}^2 + \Delta F_{\text{LR}}^2} \quad (\text{S64})$$

where ΔF_{SR} and ΔF_{LR} are the absolute real-space and Fourier-domain errors. Giving expressions for the expected error of general structures is difficult and usual error estimations assume homogenous random systems.

For all methods the real space error is?

$$\Delta F_{\text{SR}} \approx \frac{Q^2}{\sqrt{N}} \frac{2}{\sqrt{r_{\text{cut}} V}} e^{-r_{\text{cut}}^2/2\sigma^2} \quad (\text{S65})$$

where N is the number of charges, $Q^2 = \sum_{i=1}^N q_i^2$, is the sum of squared charges, and V is the volume of the system. For Ewald, the approximate force error is?

$$\Delta F_{\text{LR}}^{\text{Ewald}} \approx \frac{Q^2}{\sqrt{N}} \frac{\sqrt{2}/\sigma}{\pi \sqrt{2V/h}} e^{-2\pi^2 \sigma^2/h^2} \quad (\text{S66})$$

For PME it reads?

$$\Delta F_{\text{LR}}^{\text{PME}} \approx 2\pi^{1/4} \sqrt{\frac{3\sqrt{2}/\sigma}{N(2P+3)} \frac{Q^2}{L^2} \frac{(\sqrt{2}H/\sigma)^{P+1}}{(P+1)!}} \times \exp\left(\frac{(P+1)[\log(P+1) - \log 2 - 1]}{2}\right) \langle \phi_P^2 \rangle^{1/2} \quad (\text{S67})$$

where P is the order of the interpolation scheme, H is the spacing of mesh points, and $\phi_P^2 = H^{-(P+1)} \prod_{s \in S_H^{(P)}} (x-s)$, in which $S_H^{(P)}$ is the $P+1$ mesh points closest to the point x .

For P3M the error is?

$$\Delta F_{\text{LR}}^{\text{P3M}} \approx \frac{Q^2}{L^2} \left(\frac{\sqrt{2}H}{\sigma}\right)^P \sqrt{\frac{\sqrt{2}L}{N\sigma} \sqrt{2\pi} \sum_{m=0}^{P-1} a_m^{(P)} \left(\frac{\sqrt{2}H}{\sigma}\right)^{2m}} \quad (\text{S68})$$

where $a_m^{(P)}$ is an expansion coefficient, and its exact value can be found in Table II in Ref. ? .

Based on the error formulas above, and for a given trial structure that is representative of those most commonly used for the problem at hand, we can tune the parameters to achieve the desired accuracy following the algorithm below.

- Step 1 Based on the user given accuracy ϵ_{target} and r_{cut} , calculate the smearing σ by solving $\Delta F_{\text{SR}}(\sigma; r_{\text{cut}}) = \epsilon_{\text{target}}/2$.
- Step 2 Initialize sets of k -space parameters. For Ewald, the values are chosen such that each spatial direction (x, y, z) contains between 1 and 13 mesh points. For mesh-based methods (P3M and PME), the grid sizes range from 2 to 7 mesh points per spatial direction, considering all possible interpolation orders.
- Step 3 Evaluate all possible parameter sets. The error associated with the parameter is estimated cheaply using the error formulas. Parameters that yield error within the desired accuracy are benchmarked estimating the empirical timings for an evaluation of energy and derivatives. Parameter sets exceeding the error threshold are not tested for performance and their timings are set as infinity.
- Step 4 Return the parameter set achieving the desired accuracy with the shortest timing. If no parameter set can fulfill the accuracy requirement, the set achieving the smallest error is returned.

In Figure S6 we show the results of the tuning procedure for Ewald, PME, and P3M similarly to Fig. 3 in the main text but for double precision (64-bit) floating point numbers. As already described we find also that we achieve the requested accuracy for the Madelung constants but the accuracy saturates around 10^{-4} for Ewald summation and 10^{-5} for the mesh calculators.

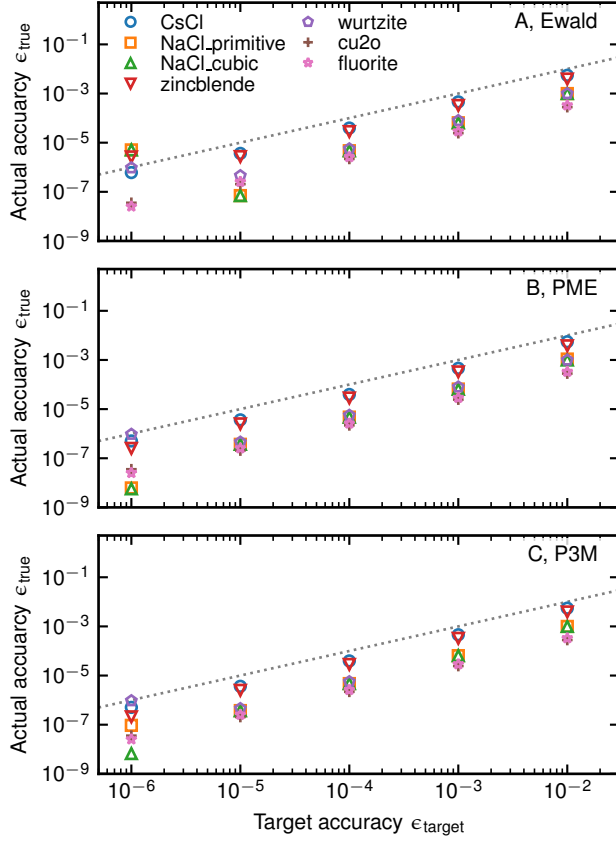


Figure S6. Similar as Fig. 3 in the main text, this figure is showing the accuracy obtained after performing the tuning procedure for a given target accuracy for different crystal structures, using double precision arithmetics. Panel A shows the results for Ewald, panel B for PME module and panel C for P3M.

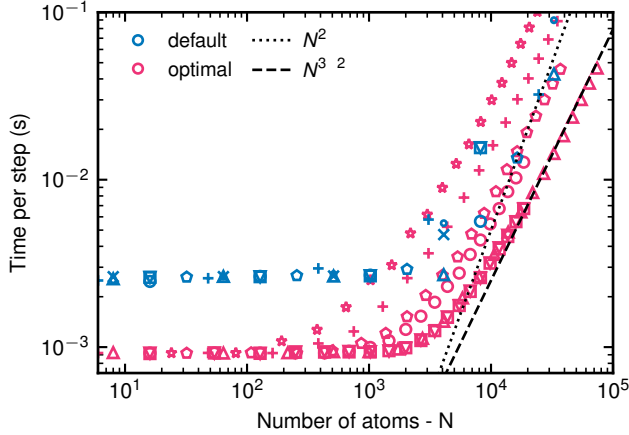


Figure S7. Benchmark for the computational costs of Ewald calculators. Blue symbols show quadratic scaling as the Ewald parameters where optimized using the procedures given above. Red symbols show $N^{3/2}$ scaling using the fixed parameters given in Equation S69.

In figure Figure S7 we show the optimal parameters for Ewald summation which leads to a scaling proportional to $N^{3/2}$ together with the quadratic scaling as it is shown in the main text in Fig. 4A. The optimal scaling was achieved by setting

$$\begin{aligned}
 \text{smearing} &= 1.3 \cdot N^{1/6} / \sqrt{2} \\
 \text{lr_wavelength} &= 2\pi \cdot \text{smearing} / 2.2 \\
 r_c &= 2.2 \cdot \text{smearing}
 \end{aligned}
 \tag{S69}$$

The parameters and pre-factors were obtained from systematic tests on a CsCl system, where the unit cell is replicated 16 times along each spatial dimension, yielding a total system of 8192 atoms.

S5. FINDING THE OPTIMAL CUTOFF FOR BENCHMARKING

To find the optimal cutoff for our benchmark simulations we perform a grid search over the real space cutoff for a replicated NaCl structure in a cubic cell. We replicated the initial cell 32 in each direction leading to a total of 262144 atoms in a cell with a side length of 64 Å. We use the same LAMMPS P3M setup as in the main text, but we only vary the real-space cutoff. Figure S8 shows the time per step versus the real space cutoff, showing the optimum efficiency is achieved for a value of 4.4 Å.

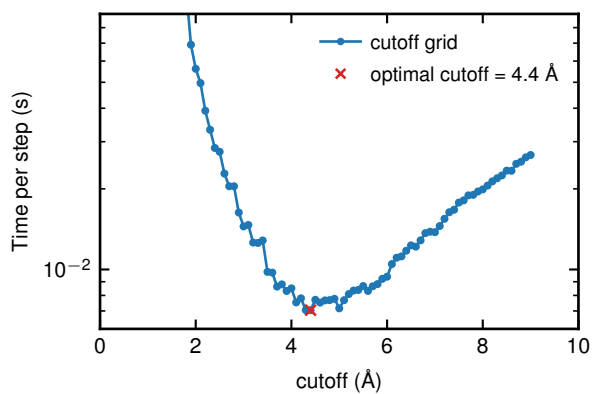


Figure S8. Time per step vs real space cutoff for replicated NaCl structure in a cubic cell. The red cross indicates the best performing cutoff of 4.4 Å.

S6. GPU UTILIZATION

During the benchmarks discussed in section IV of the main text, we collected statistics on GPU utilization (the percentage of time during which at least one kernel is executed) and power draw (power consumed by the GPU) to estimate the extent to which our code, as well as the LAMMPS reference implementation, can make use of the available hardware. The results are shown in Figure S9.

At system sizes below approximately 10000 atoms, the GPU is not fully utilized. Even at large sizes, neither our code nor LAMMPS is able to fully exhaust the available hardware, as shown by the power draw not reaching the peak design capacity of 700 W. Therefore, we expect that significant further performance improvements can be achieved by more specifically targetting specific GPUs, for instance by overlapping memory access and compute, reducing overhead, and making use of reduced-precision operations where appropriate.

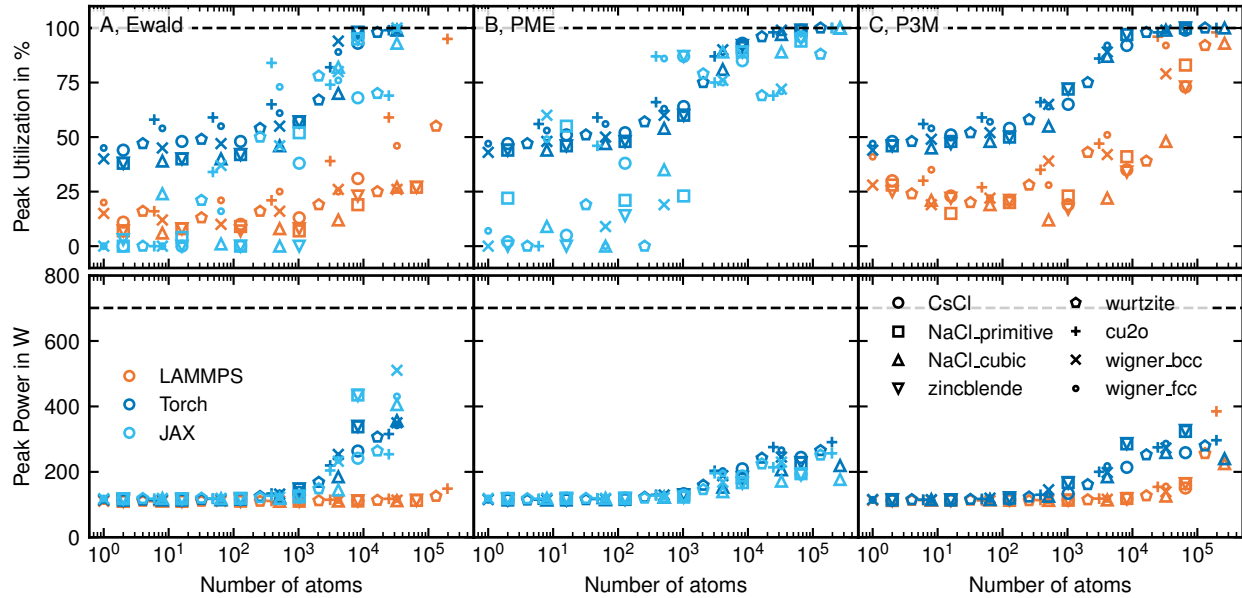


Figure S9. Upper panels: Peak percent utilization for Ewald (A), PME (B) and P3M (C) on a single NVIDIA H100 GPU. Lower panels: Peak Power in watts for the same methods. Different crystals are shown as different symbols. Each point shows the maximal utilization or power during a run of 50 single point calculations of the same positions with a tuning accuracy of $1 \cdot 10^{-4}$.

S7. MD OF WATER AT CONSTANT ENERGY AND VOLUME

Similar to the main text shown in Fig. 5, we perform MD simulations of the water system without thermostats at constant energy and volume (NVE) over 20 ps using the same settings as described in section IVB of the main text. Figure S10 shows the temperature and the energy of the system. We perform two simulations: in one, we compute the Coulomb energy in single precision (32-bit floating-point numbers), and in the other, we use double precision. In both cases, the energy is conserved, verifying that the forces are the exact derivative of the energy up to numerical precision.

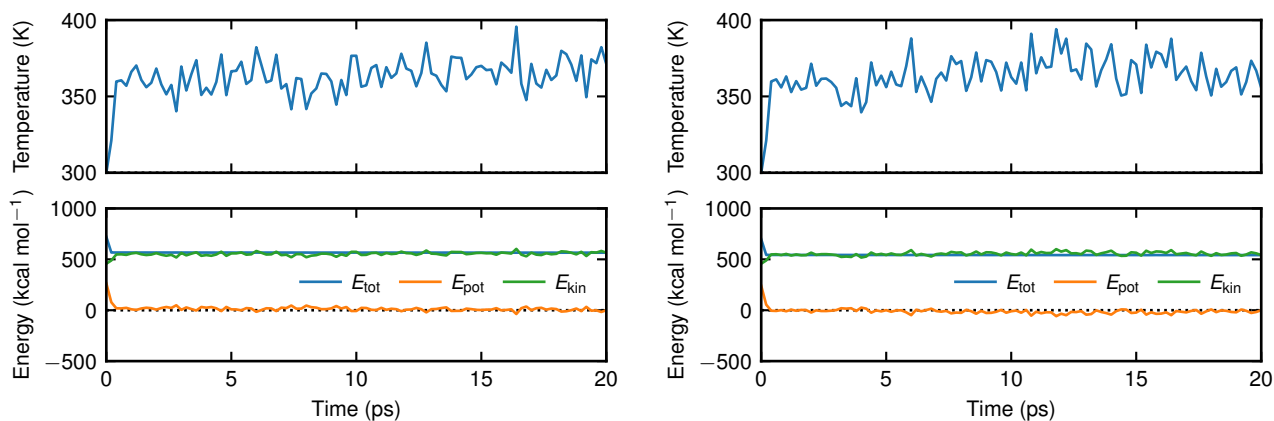


Figure S10. The temperature and the energy (split into kinetic and potential energy) of the water system in the NVE ensemble over 20 ps. The left panels show the results for the Coulomb energy computed in single precision (32-bit floating-point precision), while the right panels show the results for the Coulomb energy computed in double precision.

REFERENCES